 doi:10.20944/preprints202209.0088.v1

Article

Numerical Simulation of the Elastic-Ideal Plastic Material Behavior of Short Fiber-Reinforced Composites Including Its Spatial Distribution with an Experimental Validation

Natalie Rauter [1]*

[1] Institute of Mechanics, Helmut-Schmidt-University/University of the Federal Armed Forces Hamburg, Holstenhofweg 85, Hamburg 22043, Germany; natalie.rauter@hsu-hh.de

Abstract: For the numerical simulation of components made of short fiber-reinforced composites the correct prediction of the deformation including the elastic and plastic behavior and its spatial distribution is essential. When using purely deterministic modeling approaches the information of the probabilistic microstructure is not included in the simulation process. One possible approach for the integration of stochastic information is the use of random fields. In this study numerical simulations of tensile test specimens are conducted utilizing a finite deformation elastic-ideal plastic material model. A selection of the material parameters covering the elastic and plastic domain are represented by cross-correlated second-order Gaussian random fields to incorporate the probabilistic nature of the material parameters. To validate the modeling approach tensile tests until failure are carried out experimentally, that confirm the assumption of spatially distributed material behavior in both the elastic and plastic domain. Since the correlation lengths of the random fields cannot be determined by pure analytic treatments, additionally numerical simulations are performed for different values of the correlation length. The numerical simulations endorse the influence of the correlation length on the overall behavior. For a correlation length of 5 mm a good conformity with the experimental results is obtained. Therefore, it is concluded, that the presented modeling approach is suitable to predict the elastic and plastic deformation of a set of tensile test specimens made of short fiber-reinforced composite sufficiently.

Keywords: Short fiber-reinforced composite; Random fields; Plasticity; Numerical simulation

Citation: Rauter, N. Numerical Simulation of the Elastic-Ideal Plastic Material Behavior of Short Fiber-Reinforced Composites Including its Spatial Distribution with an Experimental Validation. *Preprints* **2022**, *1*, 0. https://doi.org/

1. Introduction

The use of short fiber-reinforced composites (SFRC) has increased significantly over the years. Due to the specific strength and stiffness in comparison to conventional polymers and the applicability for mold injection production processes they are of special interest, e.g. in the automotive industry [1]. However, the mold injection process as well as the finite length of the reinforcing elements cause a microstructure of probabilistic nature that significantly affects the mechanical properties [2] and thus the structural responds. Following this, a probabilistic modeling approach appears to be promising to exploit the lightweight potential in the best possible way.

To reduce the computational costs the main challenge here is the incorporation of microstructural information without its explicit modeling. One stochastic technique to model spatial data are random fields [3–5], that are also used in the context of material modeling. Soize and Guilleminot developed a comprehensive framework starting with non-Gaussian positive-definite matrix-valued random fields [6] and tensor-valued random fields for a meso-scale stochastic model of anisotropic elastic microstructures [7]. Based on this work by Soize the approach was extended by Guilleminot et al. covering the stochastic fluctuations in fiber-reinforced composites on the mesoscale [8,9], random interphases from atomistic simulations of polymer nanocomposites [10] and a multiscale approach for heterogeneous materials with non-Gaussian random fields [11]. Beside this random fields are widely used, e.g. for geosystems [12], thin-walled composite cylinders [13], three-dimensional concrete microstructures [14],and the representation of the continuous mode conversion observed by the propagation of guided ultrasonic waves in thin-walled

 doi:10.20944/preprints202209.0088.v1

structures made of fiber-reinforced composite [15]. A first application of random fields in the context of nonlinear behavior for isotropic material is provided by Zheng et al. [16]. The application to SFRC is limited to the linear elastic domain so far [2]. However, SFRC show prominent nonlinear behavior, because the matrix material enters the plastic domain even at operation loads [17]. Hence, to predict the structural response correctly even at low stress levels information about the plastic deformation must be considered. Since the plastic deformation are localized initially the required nonlinear modeling approach needs to include information about the probabilistic nature of the microstructure causing spatially distributed material properties [18].

Beside the work on random fields for the probabilistic material modeling, the modeling of SFRC at the different scales mostly focuses on homogenization approaches and does not consider the spatial distribution of the material properties on the component level. The determination of a representative volume element (RVE) for random composites is discussed by Savvas et al. [19] by combining the extended finite element method with a Monte Carlo sampling. Breuer et al. [20,21] applied the RVE to SFRC including artificial neural networks. Zhang et al. investigate the strain rate dependence of SFRC based on RVEs [22] and Jia et al. apply the RVE concept to cyclic mechanical and thermal loading [23].

Hence, the main objective of this research is the incorporation of the probabilistic material characteristics of SFRC into a modeling approach covering the elastic and plastic domain on the component level. The presented work is linked to a correlation structure study of the elastic-ideal plastic material behavior [24], where the moving window method [19,25,26] is utilized for the elastic domain and a homogenization method is used to derive the local apparent plastic material parameters [27,28], respectively. Here, the obtained results are now employed for the numerical simulation of SFRC on the component level including an experimental validation. Therefore, first cross-correlated random fields are generated to describe the spatial distribution and the probabilistic nature of the material properties introduced by the stochastic attributes of the microstructure. In a second step a transversely-isotropic elastic-ideal plastic material model including finite deformation is established and implemented in COMSOL Multiphysics® to simulate tensile tests for specimens made of SFRC. For validation of the presented modeling approach incorporating the spatial distribution and probabilistic characteristics of elastic and plastic material properties uniaxial tensile tests are conducted experimentally.

Subsequently, the structure of the presented work is as follows. In Section 2 the experimental investigation is given. This includes a detailed description of the specimens and the experimental setup and procedure, respectively. This is followed by the generation of cross-correlated random fields in Section 3. After the implementation of an algorithm in Multiphysics® covering elasto-plastic material behavior in Section 4, the random fields are used in Section 5 to incorporate spatially distributed material properties into the numerical modeling procedure. Finally, Section 6 gives a summary and conclusion.

2. Experiments

This section gives detailed information about the experimental investigation of the elastic and plastic properties of specimens made of SFRC by tensile tests. First, the specimen specifications are given before presenting the experimental setup and procedure. The section is concluded with an overview of the experimental results covering the elastic and plastic domain.

2.1. Specimens

In this work the elastic and plastic deformation for specimens made of Ultradur B 4300 G6 [29], a polybutylene terephthalate (PBT) matrix material filled with glass fibers, is investigated. The fiber mass fraction is set to 30%, which is equal to a fiber volume fraction of 18.2%. The specimens are cut out of a larger plate that was manufactured by mold injection. The size of this plate is 300 mm $\times$ 300 mm and has a thickness of 3 mm. The

Preprints (www.preprints.org) | NOT PEER-REVIEWED | Posted: 6 September 2022 doi:10.20944/preprints202209.0088.v1

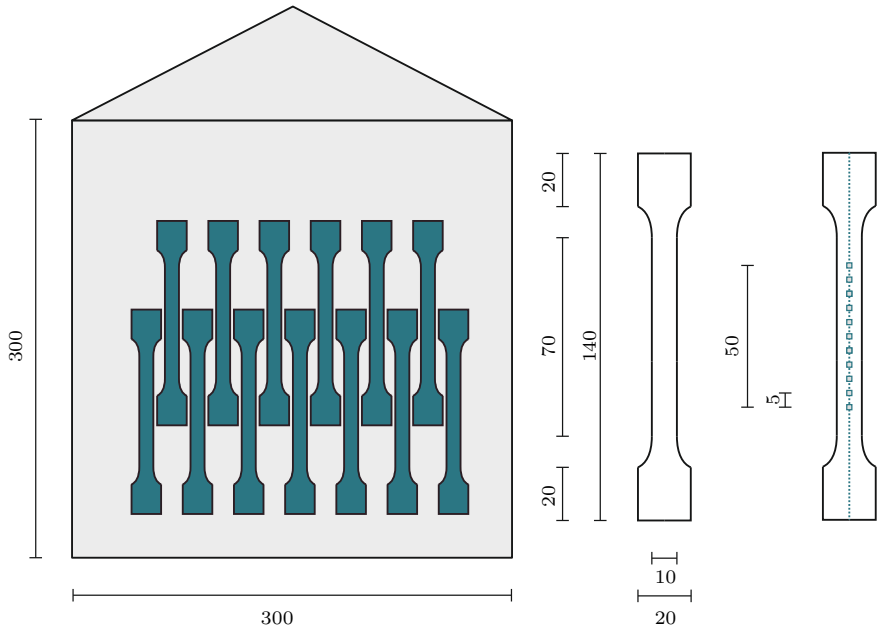

Figure 1. Details of the specimen geometry and the measurement points. All measures in mm, $t = 3\,\text{mm}$.

geometry of the tensile test specimens is defined in accordance with DIN-ISO-527-1 [30]. However, due to the plate dimensions the size of the specimen type 1B is slightly adapted. Figure 1 gives an overview of the initial plate, the position of each specimen and its exact dimensions.

2.2. Experimental setup and procedure

For the tensile tests covering the elastic and plastic deformation until failure a Zwick-Roell Z050 tensile testing machine is used. With this testing machine a load of up to 50 kN can be applied. As suggested by DIN-ISO-527-1 for plastics the tensile test is performed displacement driven with a speed of $1\,\text{mm}\,\text{min}^{-1}$. The stain is captured by a contact-less laser extensometer with an initial measurement length of 50 mm. Furthermore, to analyze the spatial distribution of the material properties additional measurement points within the original measurement length are added. They have a distance of 5 mm, see Figure 1.

For the elastic characterization of the material the Young's modulus is derived from the measured stress-strain data. It is determined by computing the slope of the curve between a strain level of 0.1% and 0.2%. For the plastic deformation the strain at failure and the maximum stress level are obtained from the measurement data. This is done based on the data for a measurement length of 50 mm for all specimens. In addition, to analyze the spatial distribution qualitatively the data is obtained for sections of 15 mm for one specimen. Hence, three non-overlapping different sections of the initial measurement length are examined individually.

2.3. Results

Figure 2 summarizes the results of the conducted tensile tests in the elastic and plastic domain. On the left hand side the stress-strain curve for each specimen based on the measurement length 50 mm is plotted. Furthermore, the diagram holds data provided by the manufacturer [29]. The stress-strain curves clearly reveal the prominent plastic deformation of SRFC even at low stress levels. However, in comparison with the data sheet the experimentally obtained stress and strain level at failure are significantly lower. This also holds for the slope of the curve in the elastic domain. For a better overview the corresponding values of the Young's Modulus as well as the stress and strain level at failure

Table 1. Experimental results obtained by tensile tests in the elastic and plastic domain.

Specimens	Number of specimens	E		σ_{failure}		$\epsilon_{\text{failure}}$	
		mean	std	mean	std	mean	std
		GPa	GPa	MPa	MPa	%	%
Experiments	8	7.95	0.87	96.1	6.22	1.97	0.14
Data sheet	1	9.69	-	135	-	2.5	-

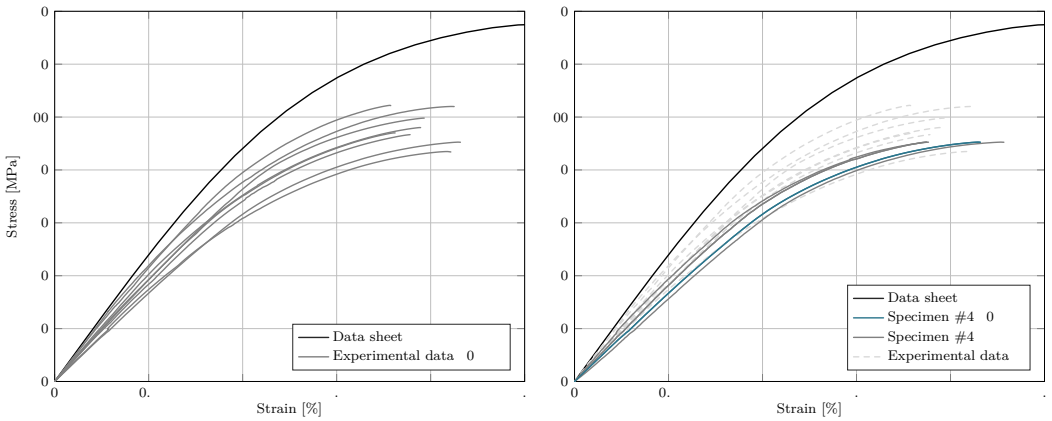

Figure 2. Experimental results and comparison with data sheet.

are collected in Table 1. For each parameter the mean value and the standard deviation are provided.

The differences between the experimental data and the data provided by the manufacturer are most likely related to the manufacturing process of the specimen. It significantly influences the microstructural characteristics like fiber length and fiber orientation of the specimen and the quality of the fiber-matrix bonding.

In the second diagram the focus is set on the spatial distribution of the material properties. For one specimen the stress-strain curve is not only determined for a measurement length of 50 mm but also for three sections of 15 mm length each. The sections don't overlap and are within the original measurement length. The different curves reveal that the plastic deformation is distributed over the specimen, confirming the assumption of spatially distributed material properties induced by the finite length of the reinforcing elements and the probabilistic characteristics of the microstructure.

3. Generation of cross-correlated random fields

In this section, first random fields and their generation by numerical methods are discussed. Afterwards, the calculation of cross-correlated random fields and their application to the problem at hand will be addressed.

3.1. Methodology

3.1.1. Random fields

Random fields $Z(\omega, \mathbf{x})$ represent spatially distributed random variables $Z(\omega)$. To describe a random field completely the function of the mean value $\mu(\mathbf{x})$, the variance $\sigma^2(\mathbf{x})$ and correlation coefficient $\rho(\mathbf{x}, \mathbf{x}')$ are required.

Utilizing random fields in the context of material modeling it is important to note, that material parameters are of positive nature. This does not necessarily apply to the coefficients of strain-energy density functions. However, it is indispensable for the yield strength, which contradicts the found normal distribution of the yield strength [24]. Therefore, when using Gaussian random fields and hence, assume normal distributed underlying random variables, negative realizations are possible [31,32]. In conclusion the use of Gaussian random fields for the representation of material properties in context of multi-

 doi:10.20944/preprints202209.0088.v1

scale modeling of heterogeneous material is controversial [6]. With non-Gaussian random fields negative realizations can be avoided and hence, a stochastic solution of second-order and the positive nature of the elasticity coefficient is guaranteed [10,11,33–36].

Non-Gaussian random fields $M(\omega, \mathbf{x})$ are defined by

$$M(\omega, \mathbf{x}) = \mathcal{G}\{Z(\omega, \mathbf{x})\}, \tag{1}$$

where $\mathcal{G}$ is a non-linear mapping operator and $Z(\omega, \mathbf{x})$ a centered, homogeneous Gaussian random field [11]. With respect to the following work, where the concept of random fields is used within the finite element method framework only discretized random fields are used, requiring a finite sampling. Consequently, as long as negative values are excluded, the difference between the results based on non-Gaussian fields and Gaussian fields may not differ significantly. Therefore, the work presented here is based on homogeneous Gaussian random fields, which also allows one to use the well-known techniques presented below.

3.1.2. Generation of random fields by numerical methods

Initially, random fields are continuous functions with respect to the spatial coordinates. However, to be able to utilize this concept within the framework of material modeling and numerical simulations by the finite element method (FEM) a discrete representation is necessary. Over the years many different methods were developed for this purpose. Examples are the midpoint method [37,38], the spatial averaging [39], and the shape function method [40–42]. Commonly used approaches are based on the series expansion technique [43]. Spanos et al. [44] extended the work by expressing random fields by a spatial decomposition of the correlation functions derived by the well-known Karhunen-Lòeve expansion (KLE) [45]. The spatial decomposition obtained by the KLE for a mean free random field with a standard deviation equal to one is given by Cho et al. [46]

$$Z(\omega, \mathbf{x}) = \sum_{n=0}^{\infty} \sqrt{\lambda_n} \phi_n(\mathbf{x}) Z_n(\omega). \tag{2}$$

Here, $Z_n(\omega)$ are uncorrelated, standard normal distributed random variables and λ_n and $\phi_n(\mathbf{x})$ are the eigenvalues and eigenfunctions of the correlation function kernel, that can be obtained by solving a Fredholm integral equation of second kind. Since the integral equation

$$\int_{\Omega} \mathrm{Cov}[\mathbf{x}', \mathbf{x}] \phi_n(\mathbf{x}) \, \mathrm{d}\, \mathbf{x} = \sum_{n=1}^{\infty} \lambda_n \phi_n(\mathbf{x}') \tag{3}$$

has closed solutions only for a few types of correlation functions defined on a rectangular domain [47], e.g. the exponential correlation function [31,48], numerical methods are often required. This is especially the case for multidimensional fields [49]. By deploying numerical integration methods the eigenfunctions $\phi_n(\mathbf{x})$ as a solution of the Fredholm integral is approximated by a set of functions h_i

$$\phi_n(\mathbf{x}') \approx \hat{\phi}_n(\mathbf{x}') = \sum_{i=1}^{N} d_i^n h_i(\mathbf{x}'), \tag{4}$$

where the parameters d_i^n are unknown and need to be determined. One technique here is the expansion optimal linear estimate (EOLE) developed by Li et al. [49]. It is based on the linear estimation theory and belongs to the group of series expansion methods. Furthermore, it can be shown that the EOLE is equivalent to the Nyström method [50] with uniform distributed integration points [47]. Within the Nyström method the integral eigenvalue problem is written as

$$\sum_{i=1}^{N} w_i \, \mathrm{Cov}[\mathbf{x}_n, \mathbf{x}_i] \hat{\phi}_j(\mathbf{x}_i) = \hat{\lambda}_j \hat{\phi}_j(\mathbf{x}_n), \tag{5}$$

Preprints (www.preprints.org) | NOT PEER-REVIEWED | Posted: 6 September 2022 doi:10.20944/preprints202209.0088.v1

which can be reorganized in matrix notation as

$$\mathbf{C}\mathbf{W}\mathbf{y}_j = \hat{\lambda}_j \mathbf{y}_j. \tag{6}$$

The $N \times N$ matrix $\mathbf{C}$ is symmetric positive semi-definite and holds the elements $c_{n,i} = \mathrm{Cov}[\mathbf{x}_n, \mathbf{x}_i]$, the integration weights w_i are stored in the diagonal matrix $\mathbf{W}$ of the size $N \times N$ and $\mathbf{y}_j$ is a column matrix with the entries $y_{j,n} = \hat{\phi}_j(\mathbf{x}_n)$. Assuming a uniform distribution of the points $\mathbf{x}_i$ over the domain Ω and a equispaced structured grid, respectively, all integration weights w_i are the same. In this case the matrix $\mathbf{W}$ reads

$$\mathbf{W} = w\mathbf{I}, \tag{7}$$

with $\mathbf{I}$ being the identity matrix and $w = |\Omega|/N$. This leads to

$$\mathbf{C}\mathbf{y}_j = \hat{\lambda}_j^* \mathbf{y}_j, \tag{8}$$

giving the equivalent of Eq. (6) for the EOLE, with the eigenvalues $\hat{\lambda}_j^*$ and eigenfunctions $\mathbf{y}_j$ of the covariance matrix $\mathbf{C}$. The eigenvalues of the EOLE are related to the eigenvalues of the Nyström method by

$$\hat{\lambda}_j^* = \frac{N}{|\Omega|}\hat{\lambda}_j. \tag{9}$$

Finally, for normalized eigenvectors the truncated KLE approximated by the EOLE reads

$$Z(\omega, \mathbf{x}) = \sum_{j=1}^{M} \frac{Z_i(\omega)}{\sqrt{\hat{\lambda}_j^*}} \sum_{i=1}^{N} y_{j,i}\, \mathrm{Cov}[\mathbf{x}, \mathbf{x}_i]. \tag{10}$$

3.1.3. Cross-correlated random fields

In the context of nonlinear material modeling the correlation is of complex nature, because the individual parameters are approximated best by different correlation functions and the parameters are strongly cross-correlated [24,51]. Therefore, to achieve a proper representation of the material properties, the generated random fields must include the information about the cross-correlation. Cho et al. introduce two different algorithms for the expansion of multi-correlated processes, namely the multiple uncorrelated Karhunen-Loève expansion (muKL) and the multiple correlated Karhunen-Loève expansion (mcKL) [46]. The main difference between these two procedures lays in the generation of the used random variables. In context of the muKL all correlated processes are described by a single set of uncorrelated random variables [46]. In contrast to this the mcKL provides multiple sets of mutually correlated random variables for the discretization of correlated processes. Since the modeling of nonlinear material behavior requires a set of random variables for each parameter the mcKL is applicable in this context.

Within this algorithm the same equations as for uncorrelated random fields are used and solved. However, in an additional step the uncorrelated random variables and eigenfunctions are transformed to obtain correlated random variables and eigenfunctions, respectively, that meet the given correlation structure. Here, first the matrix $\mathbf{K}$ is introduced. The matrix is defined as

$$K_{km}^{ij} = \mathbb{E}[Z_k^i\, Z_m^j], \tag{11}$$

where Z_k^i and Z_m^j are a set of zero-mean uncorrelated random variables for processes i and j, respectively. Using Eq. (2) the cross-covariance between the processes i and j is written as [52]

$$\begin{aligned} C_{ij} &= \mathbb{E}[f_i(\omega, \mathbf{x})\, f_j(\omega, \mathbf{y})] \\ &= \sum_{k,m=1}^{\infty} K_{km}^{ij} \sqrt{\lambda_k^i \lambda_m^j}\, \phi_k^i(\mathbf{x}) \phi_m^j(\mathbf{y}). \end{aligned} \tag{12}$$

Preprints (www.preprints.org) | NOT PEER-REVIEWED | Posted: 6 September 2022 doi:10.20944/preprints202209.0088.v1

The result is an integral equation similar to the one for the auto-correlation shown in Section 3.1.2. Following Eq. (3) the elements of $\mathbf{K}$ are obtained by solving

$$K_{km}^{ij} = \frac{1}{\sqrt{\lambda_k^i \lambda_m^j}} \int_{\Omega_1} \int_{\Omega_2} C_{ij}(\mathbf{x}, \mathbf{y}) \phi_k^i(\mathbf{x}) \phi_m^j(\mathbf{y}) \, \mathrm{d}\,\mathbf{y} \, \mathrm{d}\,\mathbf{x}. \tag{13}$$

In a final step the matrix $\mathbf{K}$ is used to determine sets of correlated random variables for each process. It is assumed that $\mathbf{K}$ is positive definite, which allows a Cholesky decomposition given by [52]

$$\mathbf{K} = \mathbf{R}\mathbf{R}^T. \tag{14}$$

Applying $\mathbf{R}$ on a set of random variables leads to

$$\tilde{\mathbf{Z}} = R^{-1}\mathbf{Z}, \tag{15}$$

where

$$\mathbb{E}[\tilde{\mathbf{Z}}\tilde{\mathbf{Z}}^T] = \mathbf{I}. \tag{16}$$

This means that $\tilde{\mathbf{Z}}$ contains only uncorrelated random variables. In reverse by applying $\mathbf{R}$ on a set of uncorrelated random variables $\tilde{\mathbf{Z}}$ gives a set of correlated random variables that represent cross-correlated random fields. The same procedure is also applicable to obtain cross-correlated eigenfunctions.

3.2. Application to the elastic-ideal plastic material behavior of SFRC

In this section the presented framework for the generation of cross-correlated random fields is used to represent the material properties of elastic-ideal plastic material behavior of SFRC. The information of the correlation structure are derived and discussed in detail by Rauter et al.study [24]. It is shown, that the correlation structure of the material parameters is approximated best by a combination of the triangle correlation function, defined as

$$\rho(\xi_1, \xi_2) = \begin{cases} a\left(1 - \frac{|\xi_1|}{b_1}\right)\left(1 - \frac{|\xi_2|}{b_2}\right) & \text{if } |\xi_1| \leq b_1, \ |\xi_2| \leq b_2 \\ 0 & \text{else} \end{cases}, \tag{17}$$

and an exponential correlation function [32,48,53]

$$\rho(\xi_1, \xi_2) = a \exp^{-\frac{|\xi_1|}{b_1} - \frac{|\xi_2|}{b_2}}. \tag{18}$$

The parameter a indicates the strength of the correlation between two parameters, ξ_1 and ξ_2 hold the spatial coordinates and b_1 and b_2 are the corresponding correlation lengths, respectively. In case of an auto-correlation a is equal to one, in case of a cross-correlation a can take values between -1 and 1.

The values of a are set in accordance with the results obtained by Rauter et al. [24]. In this initial study the numerical simulation of the elastic-ideal plastic material behavior of SFRC only two parameters are described by spatially distributed material properties to reduce the complexity of the nonlinear numerical simulations. To ensure that both the elastic and plastic domain are captured by the stochastic multiscale approach one parameter of the strain-energy density function, which is related to the elastic domain and the yield strength are represented by random fields. Based on this, the routine can be reduced to two parameters capturing the cross-correlation of Λ and σ_y. The matrix holding the factor a for each material parameter combination reads

$$\mathbf{a} = \begin{bmatrix} 1.00 & 0.53 \\ 0.53 & 1.00 \end{bmatrix}. \tag{19}$$

In addition to the parameter a the required mean values, standard deviations and correlation lengths are provided in Table 2. Since the correlation length cannot be determined

 doi:10.20944/preprints202209.0088.v1

Table 2. Mean values and standard deviations of the strain density function coefficients for a window size of 750 µm, taken from [24].

Parameter	Mean GPa	Standard deviation GPa	Correlation function	Correlation length ratio -
Λ	5.38	0.140	Triangle	1
μ	1.20	0.064	Exponential	0.4
α	1.10	0.090	Exponential	0.4
β	-0.13	0.020	Triangle	1
γ	1.13	0.148	Triangle	1
σ_y	0.126	0.015	Triangle	1

solely on numerical data, the values are normalized to the correlation length of the parameter Λ. For more details about the material model and the provided data the reader is kindly referred to Section 4.1 and the correlation analysis presented by the authors [24], respectively.

With this information at hand realizations of random fields for these two material parameters are generate using the numerical methods for two-dimensional cross-correlated homogeneous second-order random fields presented in Section 3.1. In accordance with the numerical simulation of the tensile test in Section 4 and the experimental procedure in Section 2 the domain has a size of 50 mm $\times$ 3 mm. One realization of the parameter set is presented in Figure 3. The correlation length of Λ is set to $l_x = 20$ mm and $l_y = 3$ mm in horizontal and vertical direction, respectively.

In addition, the quality of the procedure is analyzed. Therefore, in total 1000 realizations for each parameter are generated. Based on the obtained data the correlation structure is derived and compared to the results presented in the former study by the authors [24]. Figure 4 holds the results for Λ and σ_y. The first two diagrams give the analytic autocorrelation functions of Λ and σ_y, based on the results obtained in a previous correlation analysis [24], and the correlation function based on the 1000 realizations, respectively. In the last diagram the cross-correlation function is plotted. For a better overview the correlation function plots are limited to the horizontal direction. In addition to this Figure 5 gives histograms of these two parameters based on all 1000 realizations. As discussed before, in this work the material parameters are represented by Gaussian random fields. Since Gaussian random fields allow negative values in general the distribution of the sampled yield strength is analyzed more in detail. Based on the 1000 realizations and a discretization truncated after 2000 terms, in total $2e6$ values are sampled for the yield strength. The corresponding mean value and standard deviation are 125.6 MPa and 14.7 MPa, which meets the values provided in Table 2. Furthermore, the minimal and maximal sampled values are 194.7 MPa and 64.0 MPa, respectively. Since the probability density function of the yield strength was not modified to avoid negative values, the moderate standard deviation of the Gaussian distribution results only in positive realizations of the random variable. Therefore, the use of second-order Gaussian random fields appears to be appropriate to incorporate spatially distributed material properties into the numerical simulation procedure.

Subsequently, the results for the correlation functions as well as the material parameter distributions show a very good agreement with the analytic values. Hence, the selected procedure is suitable to represent the locally varying material properties of elastic-ideal plastic material behavior of SFRC by random fields.

Preprints (www.preprints.org) | NOT PEER-REVIEWED | Posted: 6 September 2022 doi:10.20944/preprints202209.0088.v1

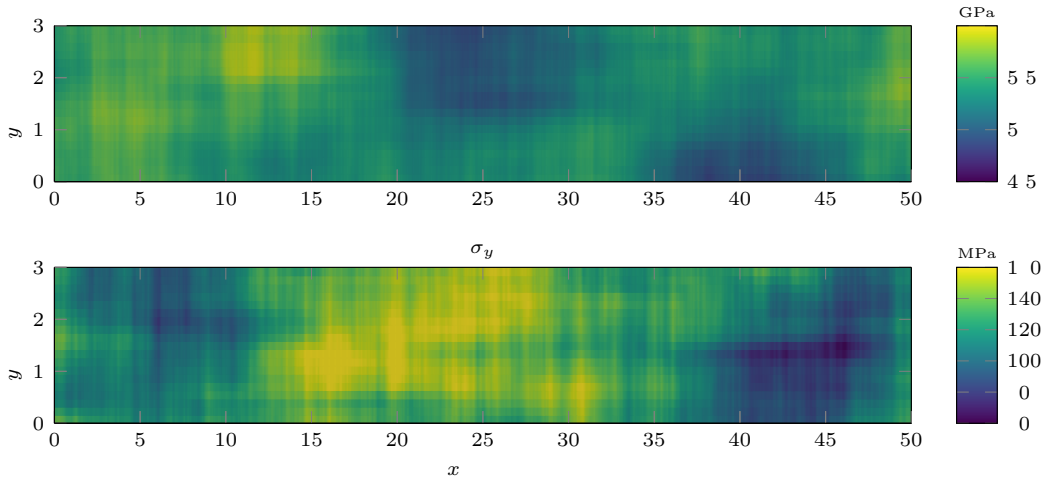

Figure 3. Representation of the spatially distributed material parameters of elastic-ideal plastic material behavior by cross-correlated homogeneous second-order Gaussian random fields.

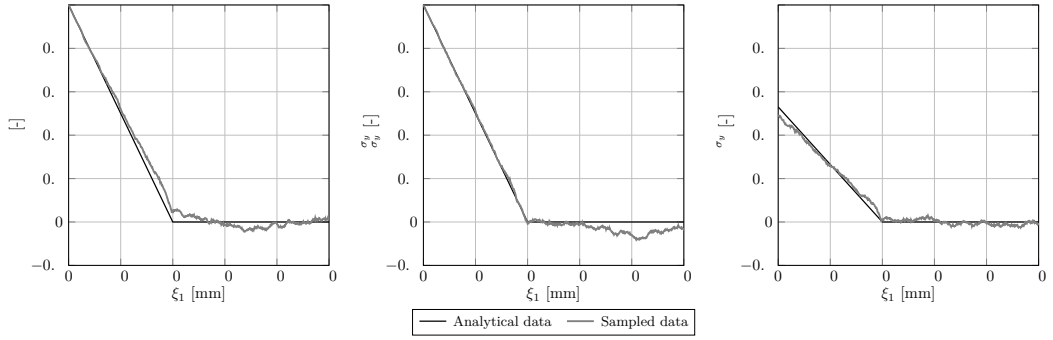

Figure 4. Correlation analysis of the generated cross-correlated random fields.

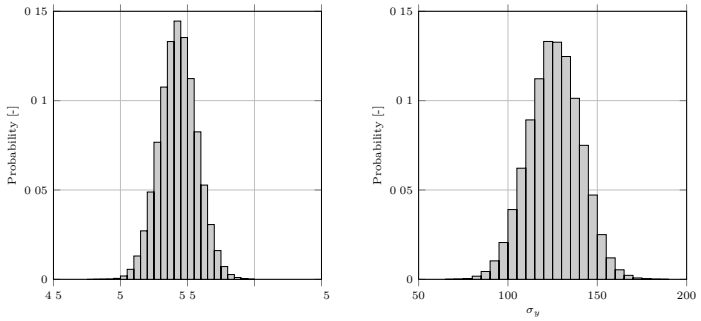

Figure 5. Histograms of the sampled values for Λ and σ_y.

4. Numerical simulation

In this section the spatially distributed material properties described by cross-correlated second-order Gaussian random fields are combined with an algorithm for elastic-ideal plastic material behavior. The main objective is the integration of the locally varying material properties, which are observed during the experimental investigations in Section 2, into a numerical modeling procedure. Therefore, first the framework and constitutive equations for transversely-isotropic elastic-ideal plastic material behavior and its implementation in COMSOL Multiphysics® is presented. The developed algorithm is then validated in detail.

Preprints (www.preprints.org) | NOT PEER-REVIEWED | Posted: 6 September 2022 doi:10.20944/preprints202209.0088.v1

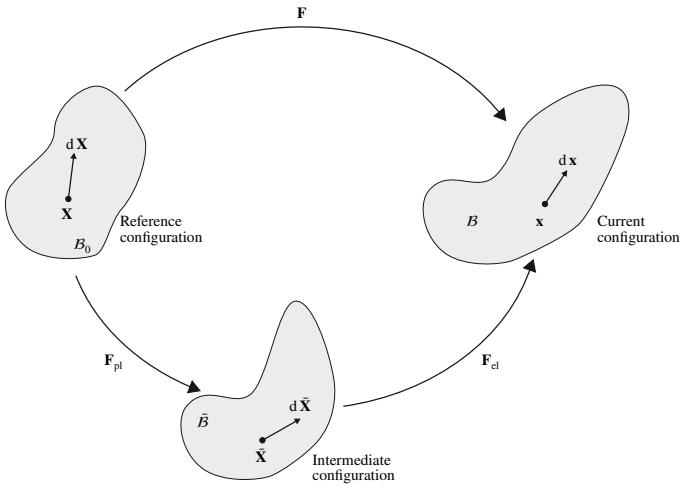

Figure 6. Configuration definition within the nonlinear continuum mechanic framework.

4.1. Framework of elastic-ideal plastic material behavior

4.1.1. Constitutive equations

The constitutive model of elastic-ideal plastic material behavior comprises the following equations

- elastic constitutive equation,
- flow rule,
- and yield condition,

which need to satisfy the Kuhn-Tucker complementary conditions and the consistency condition [54]. The plastic constitutive material model introduced here, is based on the work provided by Hashiguchi et al. [55] and Eidel et al. [56]. It is adapted to transversely-isotropic material by using the strain-energy density function by Bonet et al. [57]. Furthermore, hardening is not considered. Hence, the material is assumed to show ideal plastic behavior [24].

Since the modeling approach covers finite deformation the constitutive model needs to be formulated with respect to the nonlinear continuum mechanical framework. Therefore, the deformation is described by the multiplicative decomposition of the deformation gradient, also known as Kröner-Lee decomposition. The decomposition is given by [58–61]

$$\mathbf{F} = \mathbf{F}_{\mathrm{el}} \cdot \mathbf{F}_{\mathrm{pl}}. \tag{20}$$

Here, $\mathbf{F}_{\mathrm{el}}$ holds the elastic and $\mathbf{F}_{\mathrm{pl}}$ the plastic deformation, respectively. Since the deformation gradient is used to map continuum mechanical quantities from the reference to the current configuration and vice versa, this decomposition reveals the definition of an additional configuration, the so called intermediate configuration [54,58,60]. As shown in Figure 6, with $\mathbf{F}_{\mathrm{pl}}$ the quantities are mapped from the reference to the intermediate configuration and with $\mathbf{F}_{\mathrm{el}}$ from the intermediate to the current configuration. Accordingly

$$J = J_{\mathrm{el}} J_{\mathrm{pl}} \quad \text{with} \quad J = \det \mathbf{F} = \sqrt{\det \mathbf{C}} \tag{21}$$

holds, with $\mathbf{C} = \mathbf{F}^{\mathrm{T}} \cdot \mathbf{F}$ being the right Cauchy-Green tensor, defined in the reference configuration. It also splits into an elastic and a plastic part written by the decomposition [62]

$$\mathbf{C} = \mathbf{F}_{\mathrm{pl}}^{\mathrm{T}} \cdot \mathbf{C}_{\mathrm{el}} \cdot \mathbf{F}_{\mathrm{pl}}, \tag{22}$$

where

$$\mathbf{C}_{\mathrm{el}} = \mathbf{F}_{\mathrm{el}}^{\mathrm{T}} \cdot \mathbf{F}_{\mathrm{el}}, \qquad \mathbf{C}_{\mathrm{pl}} = \mathbf{F}_{\mathrm{pl}}^{\mathrm{T}} \cdot \mathbf{F}_{\mathrm{pl}} \tag{23}$$

 doi:10.20944/preprints202209.0088.v1

Assuming J_2-plasticity and hence, plastic incompressibility, leads to

$$\det \mathbf{C}_{\mathrm{pl}} = (J_{\mathrm{pl}})^2 = 1 \tag{24}$$

and

$$\det \mathbf{C} = J^2 = (J_{\mathrm{el}})^2 = \det \bar{\mathbf{C}}_{\mathrm{el}}, \tag{25}$$

respectively. With respect to the introduced configurations, $\bar{\mathbf{C}}_{el}$, which is located in the intermediate configuration, contains the elastic deformation whereas $\mathbf{C}_{pl}$ is assigned to the reference configuration and includes the plastic deformation.

A crucial part of the plasticity framework is the plastic flow rule providing information about the irreversible deformation of a body. The fundamental equation is the second law of thermodynamics provided by the Clausian-Duhem-inequality for isothermal processes, which is written as [63]

$$-\dot{\Psi} + \mathbf{S} : \frac{1}{2}\dot{\mathbf{C}} \geq 0, \tag{26}$$

where the dot indicates the derivative with respect to time, $\mathbf{S}$ is the second Piola-Kirchhoff stress tensor and Ψ a Helmholz free energy. Introducing a Helmholz free energy as a function of $\mathbf{C}$ the associate rate can be expressed by

$$\dot{\Psi} = \dot{\Psi}_{\mathrm{el}} = \frac{\partial \Psi_{\mathrm{el}}}{\partial \bar{\mathbf{C}}_{\mathrm{el}}} : \dot{\bar{\mathbf{C}}}_{\mathrm{el}}. \tag{27}$$

Since in this case, both kinematic and isotropic hardening are omitted, only the part Ψ_{el} of the Helmholz free energy Ψ, which is assigned to the elastic deformation, contributes to Eq. (26). Following the multiplicative decomposition of $\mathbf{F}$ the derivative of the right Cauchy-Green tensor with respect to time is obtained by [56]

$$\dot{\mathbf{C}} = \mathbf{F}_{\mathrm{pl}}^{\mathrm{T}} \cdot \left[\dot{\bar{\mathbf{C}}}_{\mathrm{el}} + 2\left(\bar{\mathbf{C}}_{\mathrm{el}} \cdot \bar{\mathbf{L}}_{\mathrm{pl}} \right)_s \right] \cdot \mathbf{F}_{\mathrm{pl}} \tag{28}$$

with the plastic velocity gradient in the intermediate configuration

$$\bar{\mathbf{L}}_{\mathrm{pl}} = \dot{\mathbf{F}}_{\mathrm{pl}} \cdot \mathbf{F}_{\mathrm{pl}}^{-1}. \tag{29}$$

Combining the inequality in Eq. (26) and the time derivative of $\mathbf{C}$, which must hold for arbitrary thermodynamic processes, one can derive first the constitutive equation for elastic deformation, which defines the second Piola-Kirchhoff stress tensor $\bar{\mathbf{S}}$ in the intermediate configuration

$$\bar{\mathbf{S}} = 2\frac{\partial \Psi_{\mathrm{el}}}{\partial \bar{\mathbf{C}}_{\mathrm{el}}} \tag{30}$$

and second the reduced form of the Clausian-Duhem inequality [56,63]

$$\bar{\mathbf{M}} : \mathbf{L}_{\mathrm{pl}} \geq 0, \tag{31}$$

again omitting isotropic and kinematic hardening. In this formulation the Mandel stress tensor $\bar{\mathbf{M}}$ is introduced. It is defined as

$$\bar{\mathbf{M}} = \bar{\mathbf{C}}_{\mathrm{el}} \cdot \bar{\mathbf{S}} \tag{32}$$

and stands in the intermediate configuration.

The inequality in Eq. (26) is satisfied by the associate flow rule [56,63]

$$\mathbf{L}_{\mathrm{pl}} = \dot{\lambda} \frac{\partial \phi}{\partial \bar{\mathbf{M}}}, \tag{33}$$

Preprints (www.preprints.org) | NOT PEER-REVIEWED | Posted: 6 September 2022 doi:10.20944/preprints202209.0088.v1

assuming an isotropic yield function ϕ [56]. In this work the framework of J_2-plasticity is used. Therefore, the yield function is introduced as a von Mises criterion by [55]

$$f_{\text{yield}} = \sqrt{\frac{3}{2}}||\bar{\mathbf{M}}_{\text{dev}}|| - \sigma_{\text{yield}}, \tag{34}$$

where σ_{yield} is the reference yield stress for uniaxial loading and hence, an independent material parameter, and $||\bar{\mathbf{M}}_{\text{dev}}||$ denotes the norm of the deviatoric part of the Mandel stress. Substituting the von Mises yield function in Eq. (34) into Eq. (33) leads to [55,63]

$$\mathbf{L}_{\text{pl}} = \dot{\lambda}\frac{\bar{\mathbf{M}}_{\text{dev}}}{||\bar{\mathbf{M}}_{\text{dev}}||}. \tag{35}$$

With this framework at hand the flow rule is written as [56]

$$\dot{\mathbf{F}}_{\text{pl}} = \mathbf{L}_{\text{pl}} \cdot \mathbf{F}_{\text{pl}} = \dot{\lambda}\frac{\bar{\mathbf{M}}_{\text{dev}}}{||\bar{\mathbf{M}}_{\text{dev}}||} \cdot \mathbf{F}_{\text{pl}}. \tag{36}$$

To solve this equation an implicit backward Euler-type tensor exponential based time integration scheme is used. Following this procedure the updated plastic part of the deformation gradient is obtained by [56,64]

$$\mathbf{F}_{\text{pl},n+1} = \mathbf{Q}_{\text{pl},n+1}\mathbf{F}_{\text{pl},n} \tag{37}$$

with the exponential function

$$\mathbf{Q}_{\text{pl},n+1} = \exp\left[\Delta\lambda\frac{\bar{\mathbf{M}}_{\text{dev},n+1}}{||\bar{\mathbf{M}}_{\text{dev},n+1}||}\right]. \tag{38}$$

The subscripts n and $n+1$ denote the corresponding steps, where n indicates the initial and $n+1$ the updated values.

The presented framework of elastic-ideal plastic deformation is applied to transversely-isotropic material behavior characterizing SFRC in a next step. Therefore, the constitutive equations are used within the context of the finite element method. The resulting routine can be divided into four steps, which are presented in detail below.

4.1.2. Solution procedure

Elastic predictor

In the initial step the deformation of the body is assumed to be purely elastic, which is described in the intermediate configuration, as shown before. Following the work of Simo et al., who derived the framework of the finite strain elasto-plasticity by combining the multiplicative decomposition of the deformation gradient with hyperelastic strain-energy density functions [65–67], the elastic deformation is obtained by evaluating the hyperelastic strain-energy density function Ψ_{el} with respect to the elastic part of the deformation.

In this study, the elastic material behavior of SFRC is described by the potential [57]

$$\begin{aligned}\Psi_{\text{el}}(\bar{\mathbf{C}}_{\text{el}}) = \frac{1}{2}\Lambda(J-1)^2 - \mu\ln(J) + \frac{1}{2}\mu\left(\operatorname{tr}\bar{\mathbf{C}}_{\text{el}} - 3\right) + \\ \left[\alpha + \beta\left(\operatorname{tr}\bar{\mathbf{C}}_{\text{el}} - 3\right) + \gamma(I_4 - 1)\right](I_4 - 1) - \frac{1}{2}\alpha(I_5 - 1).\end{aligned} \tag{39}$$

Here, Λ, μ, α, β and γ are the independent material parameters characterizing the transversely-isotropic material behavior. In addition to the well-known invariants I_1, I_2, and I_3 for the description of isotropic material behavior [68,69], the quantities I_4 and I_5 give the pseudo-invariants, which are defined for a symmetric second-order tensor $\mathbf{B}$ by [70,71]

$$I_4 = \mathbf{a} \cdot \mathbf{B} \cdot \mathbf{a} \qquad \text{and} \qquad I_5 = \mathbf{a} \cdot \mathbf{B}^2 \cdot \mathbf{a}. \tag{40}$$

Preprints (www.preprints.org) | NOT PEER-REVIEWED | Posted: 6 September 2022 doi:10.20944/preprints202209.0088.v1

The vector $\mathbf{a}$ gives the fiber orientation, and therefore, holds the transversely-isotropic characteristics of the material. In this case it is assumed, that the fibers are mainly orientated along the tensile test specimen. Hence, $a_1 = 1$ and $a_2 = a_3 = 0$ hold.

With respect to the used transversely-isotropic potential and the tensor derivatives, given by

$$\begin{aligned} \frac{\partial I_4}{\partial \mathbf{B}} &= \mathbf{a} \otimes \mathbf{a} & \frac{\partial I_5}{\partial \mathbf{B}} &= \mathbf{a} \cdot \mathbf{B} \otimes \mathbf{a} + \mathbf{a} \otimes \mathbf{B} \cdot \mathbf{a} \\ \frac{\partial \mathbf{B}}{\partial \mathbf{B}} &= \mathbb{I}^s = \frac{1}{2}(\delta_{ik}\delta_{lj} + \delta_{il}\delta_{jk}) & \frac{\partial \mathbf{B}^{-1}}{\partial \mathbf{B}} &= -\frac{1}{2}(B_{ik}^{-1}B_{lj}^{-1} + B_{il}^{-1}B_{jk}^{-1}), \end{aligned} \tag{41}$$

the second Piola-Kirchhoff stress tensor in the intermediate configuration reads

$$\begin{aligned} &\bar{\mathbf{S}} = \mu(\mathbf{I} - \bar{\mathbf{C}}_{\mathrm{el}}^{-1}) + \lambda J(J-1)\bar{\mathbf{C}}_{\mathrm{el}}^{-1} + \\ &2\beta(I_4 - 1)\mathbf{I} + 2[\alpha + \beta(\operatorname{tr}\bar{\mathbf{C}}_{\mathrm{el}} - 3) + 2\gamma(I_4 - 1)]\mathbf{a} \otimes \mathbf{a} - \alpha(\bar{\mathbf{C}}_{\mathrm{el}} \cdot \mathbf{a} \otimes \mathbf{a} + \mathbf{a} \otimes \bar{\mathbf{C}}_{\mathrm{el}} \cdot \mathbf{a}). \end{aligned} \tag{42}$$

Checking yield condition

To be able to evaluate the yield condition, provided in Eq. (34), in the intermediate configuration, the deviatoric part of the Mandel stress must be computed to derive the corresponding von Mises stress.

If the resulting von Mises stress is lower than the yield strength of the material, the body shows only elastic deformation. Therefore, no further action is required. The stress measure can be updated with the trial value obtained by the elastic predictor step. If, however, the von Mises stress is larger than the yield strength, the body shows not only elastic but also plastic deformation. In this case the determination of the resulting plastic deformation is covered by the plastic corrector step.

Plastic corrector step (return mapping)

Since the yield condition is given in the intermediate configuration, this also holds for the computation of the updated plastic part of the deformation gradient.

As shown before an associative plastic flow rule introduced by Eidel et al. [56] is used to describe the evaluation of the plastic deformation. With this framework at hand the return mapping procedure in case of plastic deformation leads to the following system of equations, cf. Eq. (37)

$$\begin{aligned} \mathbf{Y}_{\mathbf{F}_{\mathrm{pl}}} &= \mathbf{F}_{\mathrm{pl},n+1} - \mathbf{Q}_{\mathrm{pl},n+1} \cdot \mathbf{F}_{\mathrm{pl},n} = \mathbf{0}, \\ Y_{f_{\mathrm{yield}}} &= \sqrt{\frac{3}{2}\bar{\mathbf{M}}_{\mathrm{dev},n+1} : \bar{\mathbf{M}}_{\mathrm{dev},n+1}^{\mathrm{T}}} - F_{n+1} = 0, \end{aligned} \tag{43}$$

which needs to be solved to obtain the updated quantities at the step $n+1$ for the plastic deformation. Since the plastic part of the deformation gradient depends solely on the plastic multiplier $\Delta\lambda$, see Eqs. (37) and (38) a Newton-scheme algorithm is used to determine the updated components of the plastic deformation gradient. Therefore, the yield criterion is iteratively solved with respect to $\Delta\lambda$ and the procedure is stopped, when a maximum number of iterations or a converged solution is reached by satisfying the condition

$$||Y_{f_{\mathrm{yield}}}|| < \mathrm{tol}. \tag{44}$$

Furthermore, the required derivative is calculated numerically by deploying a one-sided difference scheme

$$f'(x) = \frac{f(x+h) - f(x)}{h}. \tag{45}$$

Preprints (www.preprints.org) | NOT PEER-REVIEWED | Posted: 6 September 2022 doi:10.20944/preprints202209.0088.v1

Updating

With the obtained value of $\Delta\lambda$ satisfying the yield condition the updated plastic deformation gradient $\mathbf{F}_{\mathrm{pl},n+1}$ can be calculated by evaluating Eqs. (37) and (38). Next the resulting second Piola-Kirchhoff stress tensor in the intermediate configuration is derived. Therefore, the updated elastic part of the deformation gradient is computed and introduced in Eq. (42). COMSOL Multiphysics® requires the computation of the second Piola-Kirchhoff stress tensor and the consistent tangent modulus tensor with respect to the reference configuration. Hence, a pull-back operation

$$\mathbf{S} = \mathbf{F}_{\mathrm{pl}}^{-1} \cdot \bar{\mathbf{S}} \cdot \mathbf{F}_{\mathrm{pl}}^{-\mathrm{T}}. \tag{46}$$

is applied to obtain the second Piola-Kirchhoff stress tensor in the reference configuration. The last step is the computation of the consistent tangent modulus tensor. The corresponding procedure is provided in detail in the next section.

4.1.3. Variational formulation and consistent tangent modulus tensor

For a body $\mathcal{B}$ the local form of the balance of momentum with respect to the reference configuration reads

$$\mathrm{Div}\,\mathbf{P} + \rho_0\mathbf{b} = \rho_0\ddot{u}. \tag{47}$$

Here, $\mathbf{P}$ is the first Piola-Kirchhoff stress tensor, ρ_0 is the density, $\mathbf{b}$ are the volume forces and $\mathbf{u}$ is the displacement field. To solve this differential equation Neumann and Dirichlet boundary conditions are used. They are given by

$$\mathbf{u} = \bar{\mathbf{u}} \text{ on } \partial\mathcal{B}_{\sqcap} \tag{48}$$

$$\mathbf{P} \cdot \mathbf{N} = \bar{\mathbf{t}} \text{ on } \partial\mathcal{B}_{\sigma}, \tag{49}$$

where $\partial\mathcal{B}$ is the boundary surface of $\mathcal{B}$ and $\mathbf{N}$ gives the normal to the boundary surface $\partial\mathcal{B}_{\sigma}$. To ensure, that the boundary conditions cover the complete surface of the body $\partial\mathcal{B} = \partial\mathcal{B}_{\sqcap} \cup \partial\mathcal{B}_{\sigma}$ and $\partial\mathcal{B}_{\sqcap} \cap \partial\mathcal{B}_{\sigma} = \emptyset$ hold. Applying standard variational calculus on Eq. (47) and $\mathbf{P} = \mathbf{F} \cdot \mathbf{S}$ leads to

$$F(\mathbf{u}, \delta\mathbf{u}) = \int_{\mathcal{B}} \frac{1}{2}\mathbf{S} : \delta\mathbf{C}\mathrm{d}V + \int_{\mathcal{B}} \rho_0(\ddot{\mathbf{u}} - \mathbf{b}) \cdot \delta\mathbf{u}\mathrm{d}V - \int_{\partial\mathcal{B}_{\sigma}} \bar{\mathbf{t}} \cdot \delta\mathbf{u}\mathrm{d}S = 0 \tag{50}$$

for the equilibrium state of the body $\mathcal{B}$. Based on the definition

$$\mathbf{C} = \mathbf{F}^{\mathrm{T}} \cdot \mathbf{F} \tag{51}$$

the virtual right Cauchy-Green deformation tensor, expressed with respect to the virtual deformation gradient $\delta\mathbf{F} = \mathrm{Grad}\,\delta\mathbf{u}$, is given by

$$\delta\mathbf{C} = (\delta\mathbf{F}^{\mathrm{T}} \cdot \mathbf{F} + \mathbf{F}^{\mathrm{T}} \cdot \delta\mathbf{F}). \tag{52}$$

To solve this nonlinear equation within the FEM framework a standard Newton-Raphson iteration scheme is used. To ensure a quadratic convergence rate a consistent linearization of the principal of virtual displacement in Eq. (50) is crucial. Therefore, in this work the pertubation technique developed by Miehe [72] is used. This approach is widely in use and has been extensively investigated with respect to convergence properties and the application within the finite strain framework [56,73,74]. Due to the symmetry of $\mathbf{S}$ the linear increment of F can be formulated as

$$\Delta F(\mathbf{u}, \delta\mathbf{u}, \Delta\mathbf{u}) = \frac{1}{2}\int_{\mathcal{B}} (\delta\mathbf{C} : \Delta\mathbf{S} + \Delta\delta\mathbf{C} : \mathbf{S})\mathrm{d}V, \tag{53}$$

where $\Delta\delta\mathbf{C} = (\Delta\mathbf{F}^{\mathrm{T}} \cdot \delta\mathbf{F} + \delta\mathbf{F}^{\mathrm{T}} \cdot \Delta\mathbf{F})$ is the linearized virtual right Cauchy-Green deformation tensor given in terms of the incremental deformation gradient $\Delta\mathbf{F} = \mathrm{Grad}\,\Delta\mathbf{u}$.

Preprints (www.preprints.org) | NOT PEER-REVIEWED | Posted: 6 September 2022 doi:10.20944/preprints202209.0088.v1

To obtain the incremental second Piola-Kirchhoff stress tensor $\Delta\mathbf{S}$ the consistent tangent modulus tensor is required. In the reference configuration it is expressed by

$$\mathbb{C} = 2\frac{\partial \mathbf{S}}{\partial \mathbf{C}}, \tag{54}$$

which can be written as

$$\mathbb{C} = 2\frac{\Delta \mathbf{S}}{\Delta \mathbf{C}} = \sum_{i,j,k,l=1}^{3} 2\frac{\Delta S_{ij}}{\Delta C_{kl}} \mathbf{E}_i \otimes \mathbf{E}_j \otimes \mathbf{E}_k \otimes \mathbf{E}_l. \tag{55}$$

The incremental change of the right Cauchy-Green tensor is obtained by applying a pertubation technique to the deformation gradient. Following this, the incremental change of the right Cauchy-Green tensor is given by

$$\Delta\mathbf{C} = \Delta\left(\mathbf{F}^{\mathrm{T}} \cdot \mathbf{F}\right) = \mathbf{F}^{\mathrm{T}} \cdot \Delta\mathbf{F} + (\Delta\mathbf{F})^{\mathrm{T}} \cdot \mathbf{F} \tag{56}$$

with

$$\Delta\mathbf{F}_{kl}(\epsilon) = \frac{\epsilon}{2}\left\{\left(\mathbf{F}_{\mathrm{n+1}}^{-\mathrm{T}} \cdot \mathbf{E}_k\right) \otimes \mathbf{E}_l + \left(\mathbf{F}_{\mathrm{n+1}}^{-\mathrm{T}} \cdot \mathbf{E}_l\right) \otimes \mathbf{E}_k\right\}. \tag{57}$$

Subsequently, the perturbed deformation gradient reads

$$\mathbf{F}_{\mathrm{n+1}}(\epsilon) = \mathbf{F}_{\mathrm{n+1}} + \Delta\mathbf{F}(\epsilon). \tag{58}$$

With this the corresponding perturbed incremental right Cauchy-Green tensor can be calculated, which enables one to compute the stresses by applying the presented return mapping algorithm. This leads to the stress increment

$$\Delta\mathbf{S} = S(\mathbf{F}_{\mathrm{n+1}}(\epsilon)) - S(\mathbf{F}_{\mathrm{n+1}}) \tag{59}$$

and hence, the consistent tangent modulus tensor by evaluating Eq. (55)

4.2. Implementation in COMSOL Multiphysics®

4.2.1. Algorithm

Using an external material option in COMSOL Multiphysics® requires the generation of a C-based dll, which can be loaded via the COMSOL Multiphysics® interface. With respect to the presented elastic-ideal plastic material model introduced in Section 4.1 the general stress deformation routine is used. The input and output parameter for a general stress deformation subroutine for the implementation in COMSOL Multiphysics® are provided in Table 3. In addition to these variables optional ones can be stored utilizing state variables. Table 4 gives an overview of the state variables used in the presented algorithm for the elastic-ideal plastic material behavior of SFRC.

With these definitions and the framework provided in Section 4.1 an algorithm is established to compute the second Piola-Kirchhoff stress tensor and the Jacobian matrix of the second Piola-Kirchhoff stress tensor with respect to deformation gradient. The structure of the developed routine is depicted in Figure 7. The main routine EVAL reads the input variables, calls the subroutine RETMAP, which is responsible for the return mapping procedure and updates all output and state variables. A detailed overview of the routine is provided by Algorithm 1. In addition Algorithm 2 and Table 5 hold all information about the subroutine RETMAP. Details of all remaining supporting routines indicated in Figure 7 are given in Appendix A.

4.2.2. Validation of the algorithm

For the validation process a two-dimensional numerical model under plane strain assumption representing the cross-section of a tensile test specimen is used. The size of the numerical model is 50 mm × 3 mm. In Figure 8 the numerical model and the

Preprints (www.preprints.org) | NOT PEER-REVIEWED | Posted: 6 September 2022 doi:10.20944/preprints202209.0088.v1

Table 3. List of input and output variables for a general stress deformation routine in COMSOL Multiphysics®.

Variable	Symbol	Description
`FlOld`	$\mathbf{F}_n$	Input: Deformation gradient at previous step
`Fl`	$\mathbf{F}_{n+1}$	Input: Deformation gradient at current step
`tempOld`	$\mathbf{T}_n$	Input: Temperature at previous step
`temp`	$\mathbf{T}_{n+1}$	Input: Temperature at current step
`K`	$\mathbf{e}$	Input: Local material coordinate system
`delta`	–	Input: reserved for future use
`nPar`	n	Input: Number of material model parameters
`par`	–	Input: Array with the material model parameters
`sPK`	$\mathbf{S}_{n+1}$	Output: Second Piola-Kirchhoff stress tensor given in Voigt order
`J`	$\mathbf{J}$	Output: Jacobian of stress with respect to deformation gradient as a 6-by-9 matrix of partial derivatives of components of `sPK` with respect to components of `F`

Table 4. List of state variables used in the algorithm for the elastic-ideal plastic material behavior in COMSOL Multiphysics®.

Variable	Symbol	Description
`nStates1`	–	Input: Size of state array
`states1`	$\mathbf{F}_{\mathrm{pl},n}$	Input: Plastic part of deformation gradient at previous step

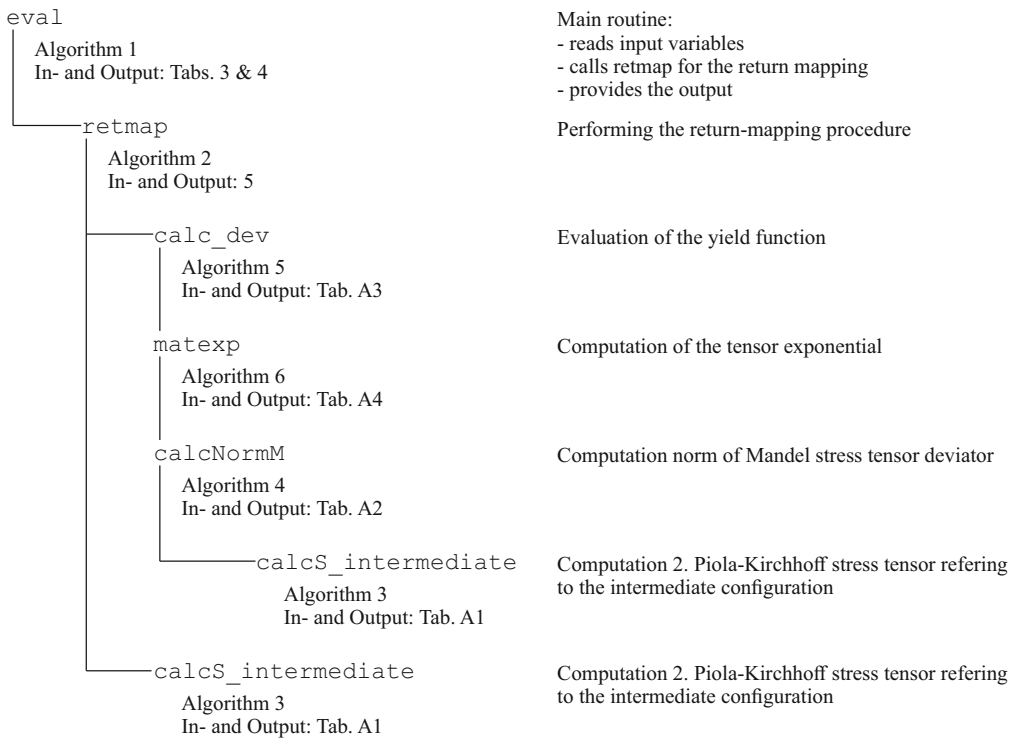

Figure 7. Structure of the implemented algorithm.

Preprints (www.preprints.org) | NOT PEER-REVIEWED | Posted: 6 September 2022 doi:10.20944/preprints202209.0088.v1

Algorithm 1 Main routine implemented in COMSOL Multiphysics® for the calculation of $\mathbf{S}$ and $\mathbf{J}$

Input: see Tables 3 and 4
Output: see Tables 3 and 4

procedure EVAL
  read material parameters
  read state variables
  initialize Jacobian and identity matrix
  compute $\bar{\mathbf{S}}_{n+1}$ in intermediate configuration and $\mathbf{F}_{\mathrm{pl},n+1}$ calling Alg. 2 ▷ Eq. (42)
  compute $\mathbf{S}_{n+1}$ by pull back of $\bar{\mathbf{S}}_{n+1}$ ▷ Eq. (46)
  save $\mathbf{S}_{n+1}$ in Voigt notation
  update state variable $\mathbf{F}_{pl,n+1}$
  compute perturbed deformation gradient $\Delta\mathbf{F}(\epsilon)$ ▷ Eq. (57)
  compute $\bar{\mathbf{S}}_{n+1}$ in intermediate configuration ▷ Eq. (42)
  compute $\mathbf{S}_{n+1}$ by pull back of $\bar{\mathbf{S}}_{n+1}$ ▷ Eq. (46)
  compute Lagrangian consistant tangent modulus tensor ▷ Eq. (55)
  reorganize $\mathbb{C}$ in Voigt notation
  compute Jacobian by calling COMSOL Multiphysics® utilize function `csext_jac_con`
  return
end procedure

Algorithm 2 Return-mapping algorithm implemented in COMSOL Multiphysics® for the calculation of $\bar{\mathbf{S}}$ and $\mathbf{F}_{\mathrm{pl}}$

Input: see Table 5
Output: see Table 5

procedure RETMAP
  compute $||\bar{\mathbf{M}}_{\mathrm{dev}}||$ by calling Alg. A2
  evaluate yield condition by calling Alg. A3 ▷ Eq. (34)
  if $f_{\mathrm{yield}} > 0$ **then**
    initialize Newton iteration
    evaluate yield condition for current value of $\Delta\lambda$ by calling Alg. A3 ▷ Eq. (34)
    while $||f_{\mathrm{yield}}|| \geq 1e-4$ and $n_{\mathrm{iter}} \leq n_{\max}$ **do**
      compute $\Delta\lambda + \epsilon$
      evaluate yield condition for current value of $\Delta\lambda + \epsilon$ by calling Alg. A3 ▷ Eq. (34)
      compute $\frac{\partial f_{\mathrm{yield}}}{\partial \Delta\lambda}$ by numerical differentiation
      update $\Delta\lambda$
      evaluate yield condition for updated value of $\Delta\lambda$ by calling Alg. A3 ▷ Eq. (34)
    end while
    compute $||\bar{\mathbf{M}}_{\mathrm{dev}}||$ by calling Alg. A2 for final value of $\Delta\lambda$
    compute directional tensor for plastic evolution
    compute tensor exponential by calling Alg. A4 ▷ Eq. (38)
    update $\mathbf{F}_{\mathrm{pl}}$ ▷ Eq. (37)
  end if
  compute $\mathbf{F}_{\mathrm{el}}$ ▷ Eq. (20)
  compute $\mathbf{C}$ ▷ Eq. (51)
  compute $\bar{\mathbf{S}}_{n+1}$ in intermediate configuration by calling Alg. A1 ▷ Eq. (42)
  return
end procedure

Preprints (www.preprints.org) | NOT PEER-REVIEWED | Posted: 6 September 2022 doi:10.20944/preprints202209.0088.v1

Table 5. List of input and output variables for the subroutine RETMAP COMSOL Multiphysics®.

Variable	Symbol	Description
`F`	$\mathbf{F}$	Input: Deformation gradient
`Fpl`	$\mathbf{F}_{\mathrm{pl},n}$	Input: Plastic part of deformation gradient
`Fpl`	$\mathbf{F}_{\mathrm{pl},n+1}$	Output: Updated plastic part of deformation gradient
`Sint`	$\bar{\mathbf{S}}$	Output: Second Piola-Kirchhoff stress tensor with respect to the intermediate configuration
`lam`	Λ	Input: Material parameter
`mu`	μ	Input: Material parameter
`alpha`	α	Input: Material parameter
`beta`	β	Input: Material parameter
`gamma`	γ	Input: Material parameter
`sigYs`	σ_{yield}	Input: Yield stress

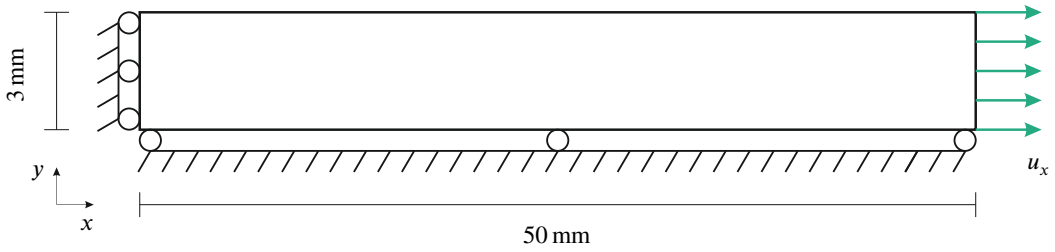

Figure 8. Two-dimensional numerical model.

corresponding boundary conditions are depicted. To reduce convergence issues during the plastic deformation the simulation is displacement driven. Beside that, the numerical model is discretized by 4-node-elements with a size of 0.25 mm × 0.25 mm. Hence over the thickness the cross-section is discretized with 12 and along the cross-section with 200 elements.

Due to the fact, that COMSOL Multiphysics® experiences some issues when combining a user-defined hyperelastic strain-energy density function with plasticity the provided algorithm is validated in two steps. In a first step the external material algorithm is validated based on the well-known hyperelastic Neo-Hookean material model [75]. Therefore, the strain-energy density function within the presented algorithm is adapted to the one implemented in COMSOL Multiphysics® for the Neo-Hookean material model given by

$$\Psi_{\mathrm{Neo}} = \frac{1}{2}\mu(I_1 - 3) - \mu\ln(J) + \frac{1}{2}\Lambda[\ln(J)]^2. \tag{60}$$

Subsequently two numerical simulations are performed. One with the implemented Neo-Hookean hyperelastic material model and a second one with the provided external material algorithm. In both cases ideal plasticity and a plain-strain state are assumed. The corresponding material properties are provided in Table 6. Furthermore, a total displacement of $u_x = 1\,\mathrm{mm}$ corresponding to a strain of 2% is applied to ensure plastic deformation. In a second step the strain-energy density function provided by Bonet et al. [57] is passed to COMSOL Multiphysics® as an user-defined potential. Since this cannot be be combined with ideal plastic behavior due to convergence issues, this is only simulated assuming elastic deformation. The results are compared again to the results provided by Algorithm 1. The corresponding material parameters are also provided in Table 6.

The results are depicted in Figure 9. The first row gives the result for the isotropic Neo-Hookean simulation, the second row holds the results for the transversely-isotropic simulations. The diagrams on the left hand side contain stress-strain curves. The von Mises stress is plotted in black and the horizontal component of the second Piola-Kirchhoff stress is plotted in gray, respectively. Following the theoretical framework provided in Section 4.1 it is important to note, that the von Mises stress is given in the intermediate configuration

Preprints (www.preprints.org) | NOT PEER-REVIEWED | Posted: 6 September 2022 doi:10.20944/preprints202209.0088.v1

Table 6. Material parameters validation with Neo-Hookean material model.

	Λ GPa	μ GPa	α GPa	β GPa	γ GPa	σ_Y MPa
Neo-Hookean	5.38	1.20	-	-	-	50
Transversely-isotropic	5.38	1.20	1.10	-0.13	1.13	-

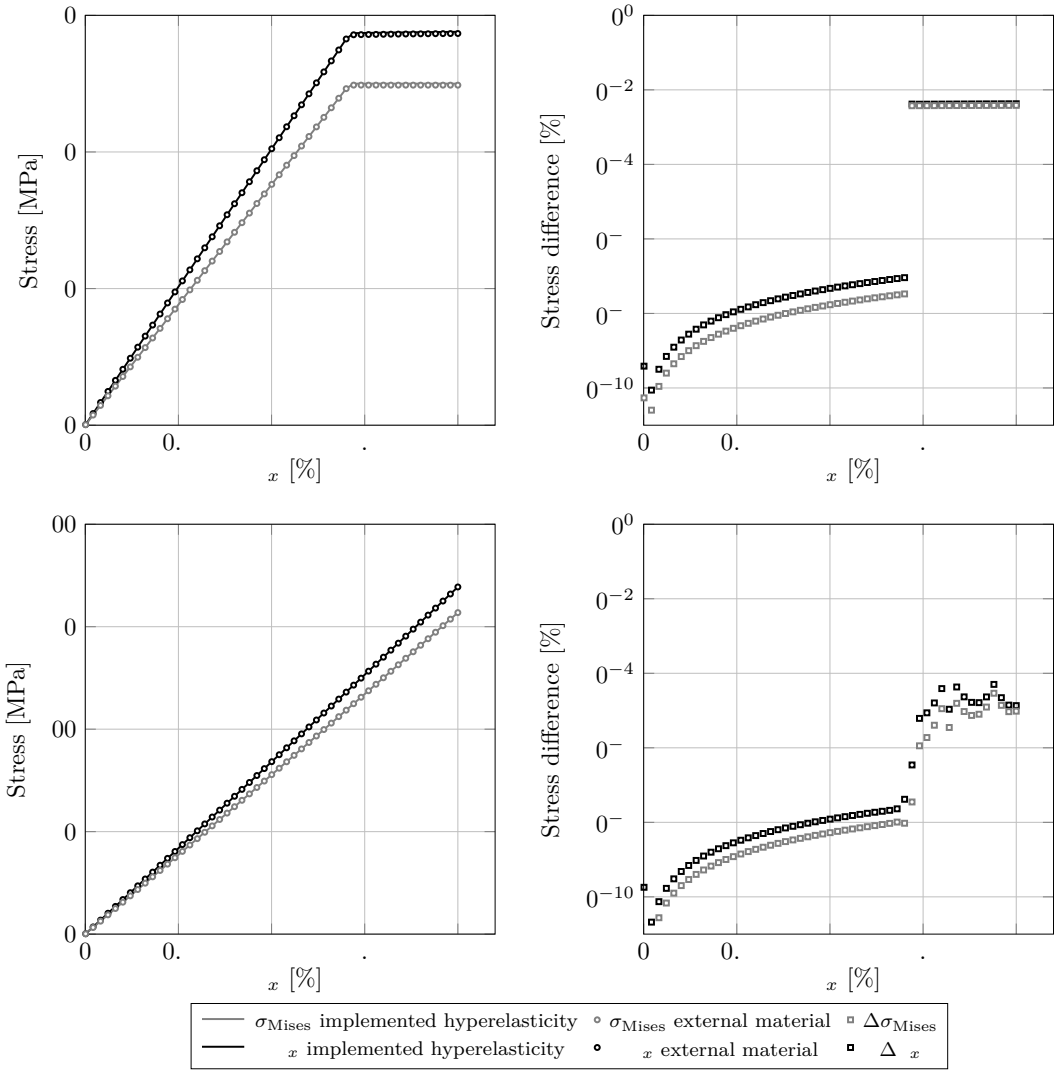

Figure 9. Numerical validation of the implemented general stress-deformation algorithm in COMSOL Multiphysics®.

 doi:10.20944/preprints202209.0088.v1

where as the second Piola-Kirchhoff stress tensor stands in the reference configuration. The solid lines give the results of the implemented material model in COMSOL Multiphysics® and the small circles belong to the results obtained by the external material routine. As indicated by the diagrams on the right hand side, that provide the deviation of the external material routine to the implemented material model in percent, both validation steps show good agreement. Both comparisons experiences an increasing deviation at large displacements, which is still very small.

5. Application to tensile test specimen

In this last step the presented modeling approach is used to incorporate the spatial distributed elastic-ideal plastic material behavior of SFRC into a numerical simulation of tensile tests. As mentioned before the probabilistic characteristics of the material parameters are analyzed in a former study of the authors [24]. The main results are summarized in Table 2 for a window size of 750 µm, which show the best approximation for the simulation on the component level [76]. In this section the numerical model is briefly introduced, the numerical results are shown and corresponding results are discussed in detail including a comparison with the experimental data presented in Section 2. This includes the analysis of the influence of the correlation length on the standard deviation of the obtained results and the selection of an optimal correlation length for which the numerical results and the experimental measurements coincide best.

5.1. Numerical model

The numerical model used to validate the novel modeling approach on the component level based on tensile test specimens is identical to the one used in Section 4.2.2. As already discussed in Section 3.2 only one parameter of the strain-energy density function and the yield strength are represented by cross-correlated second-order Gaussian random fields. This reduces the complexity at this state of the investigations. Since in this case the standard deviation of the material parameter Λ does not cover the total standard deviation of elasticity tensor element C_{11}, which is significantly related to the structural behavior under uniaxial tension, the corresponding value is set to 1.74 GPa. Furthermore, the experimental data clearly reveal that local plastic deformation occur even at low stress levels. This is related to the yield strength of the matrix material and to plastic deformation induced by stress peaks at the edges of the reinforcing elements. In addition, the maximal stress level of the data sheet and hence, the results of the homogenization is not reached. Therefore, the mean value and the standard deviation are adjusted and set to 100 MPa and 31 MPa, respectively. The remaining parameters are assumed to be homogeneous and are set to the mean values obtained by a previous correlation analysis [24]. Furthermore, a plain strain state is employed. This is eligible because the microstructure of SFRC consists of layers with different main fiber orientation [77,78]. The core layer, which is located in the center of the cross-section, is characterized by a fiber orientation perpendicular to the main flow direction of the injection mold process. With respect to the specimens used in this study the fibers within the small core layer are perpendicular to the load direction and hence, inhibit the out-of-plane deformation.

Further crucial parameters for the numerical simulation are the correlation lengths of the random fields. Since the correlation length significantly influences the local distribution of the material properties it is strongly linked to the standard deviation of the numerical results. Therefore, in this study different values are used to analyze the influence more in detail. In Figure 10 realizations for the strain-energy density function parameter Λ are depicted for a correlation length in horizontal direction of $l_x = 5\,\text{mm}$, $l_x = 10\,\text{mm}$, and $l_x = 20\,\text{mm}$. In vertical direction the correlation length is set to $l_y = 3\,\text{mm}$. The effect of the correlation length on the random field is clearly observable. In analogy to the description of oscillations the correlation length can be interpreted as the wavelength of the dominant eigenfunctions.

Preprints (www.preprints.org) | NOT PEER-REVIEWED | Posted: 6 September 2022 doi:10.20944/preprints202209.0088.v1

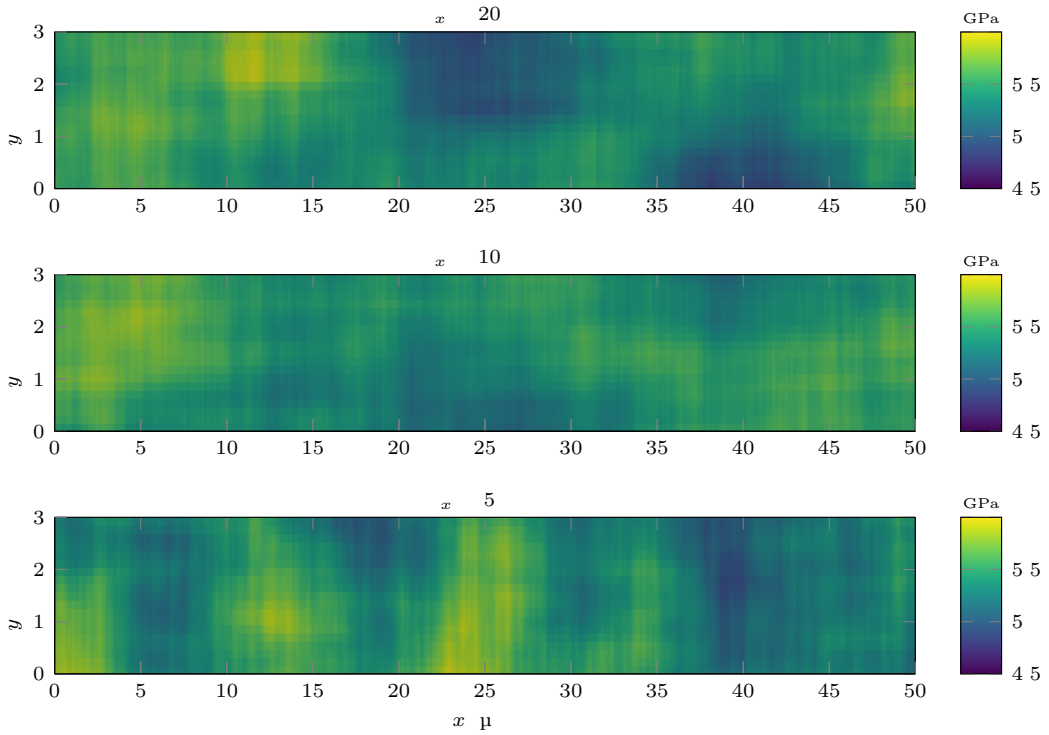

Figure 10. Discretizations of cross-correlated homogeneous second-order Gaussian random fields to represent the spatially distributed material parameter Λ for different values of l_x.

In this work the numerical simulation are performed for horizontal correlation length of $l_x = 5\,\text{mm}$, $l_x = 10\,\text{mm}$, and $l_x = 15\,\text{mm}$. The correlation length in vertical direction is set to 0.3 mm for all simulations. The value is chosen to allow plastic deformation at different locations as it is observed during the experimental investigations. In combination with the ideal plastic modeling approach the resulting stress-strain relation approximates the experimental data for reinforced material. Would the correlation length be identical to the specimen's thickness of 3 mm the plastic deformation is limited to the region where the yield strength is reached first, because the surrounding material cannot take higher stress levels. The obtained results would then be characterized purely by the ideal plastic behavior of the matrix material.

The numerical simulations are carried out for eight different realizations per correlation length. Hence, in total 24 simulations are conducted. The results are presented below.

5.2. Results

The results of the numerical simulations are summarized in Figure 11. Furthermore, a comparison of the numerical data with the experimental results is included. The diagrams on the left hand side contain the stress-strain curve (black), taken from the data sheet [29], the experimental data (gray), see Section 2, and the numerically obtained results (colored) for correlation lengths of $l_x = 5\,\text{mm}$, $l_x = 10\,\text{mm}$, and $l_x = 15\,\text{mm}$ from top to bottom. The diagrams on the right hold again the stress-strain curve (black), taken from the data sheet [29] and the numerical data (gray). One data set is highlighted. The corresponding stress-strain curve is based on a measurement length of 50 mm. For these specimens the spatial distribution of the material properties is qualitatively investigated by deriving the results for three sections of 15 mm each.

For a better comparability Table 7 holds some additional information. For strain levels of 0.2 %, 0.5 %, 1.0 %, 1.5 %, and 2.0 % the mean stress as well as standard deviations are computed for the numerical and experimental data. For all numerical results the stress refers to the horizontal component of the second Piola-Kirchhoff stress tensor.

Preprints (www.preprints.org) | NOT PEER-REVIEWED | Posted: 6 September 2022 doi:10.20944/preprints202209.0088.v1

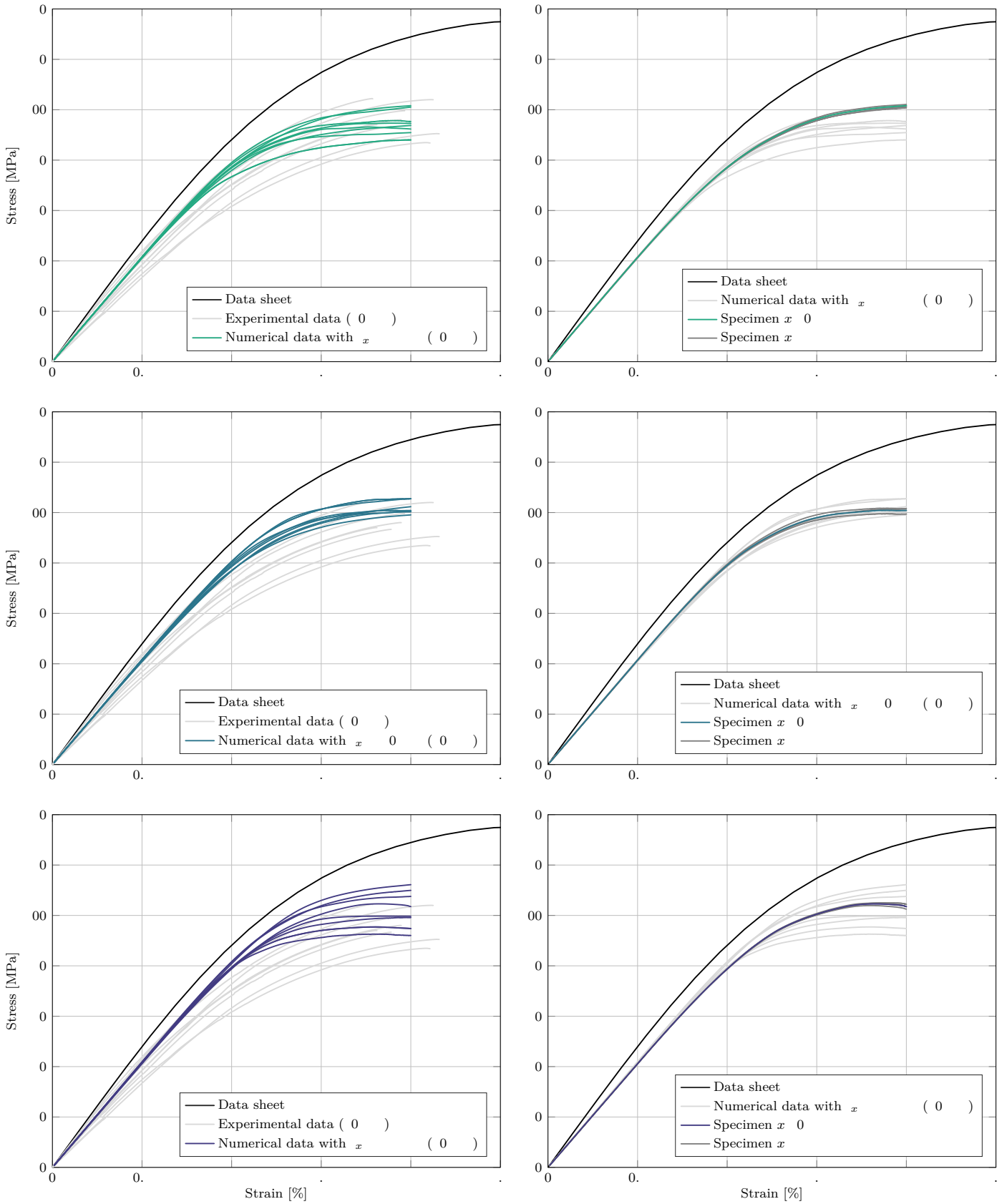

Figure 11. Results of the numerical simulation in comparison with the experimentally obtained results and a stress-strain curve provided by the manufacturer [29].

 doi:10.20944/preprints202209.0088.v1

Table 7. Deviation of the second Piola-Kirchhoff stress tensor component for the examined correlation lengths at different strain levels and comparison with the experimental data.

Strain level	$l_x = 15\,mm$		$l_x = 10\,mm$		$l_x = 5\,mm$		Experimental data	
	mean	std	mean	std	mean	std	mean	std
	MPa	MPa	MPa	MPa	MPa	MPa	MPa	MPa
0.2	16.6	0.1	16.6	0.1	16.6	0.1	16.1	1.8
0.5	41.6	0.3	41.4	0.3	41.3	0.2	38.7	3.7
1.0	80.0	1.2	78.6	1.6	76.9	1.7	70.0	5.8
1.5	99.2	5.2	97.7	2.6	92.0	3.9	88.5	6.8
2.0	102.3	7.2	101.8	2.4	94.7	4.9	95.8	6.3

5.3. Discussion

The diagrams provided in Figure 11 reveal that the numerical obtained stress-strain curves clearly show the expected elasto-plastic behavior. Despite the fact, that the material behavior is modeled based on the assumption of an elastic ideal-plastic material model, the resulting stress-strain curves show an overall good agreement with the experimental data. This is related to the localized plastic deformation and the rearrangement of the applied loading. In addition the diagrams disclose, that the numerical results show a better agreement with the experimental data for a decreasing correlation length. This is also indicated by the values provided in Table 7. For a decreasing correlation length the mean stress state converges to the experimentally obtained values, for a correlation length of 5 mm the results show an overall good agreement. The deviation between the mean stress states at the different strain levels for the experimental and numerical results is covered by the standard deviation. However, despite the good overall conformity, the results indicate two shortcomings. First, the experimentally obtained stress range at strain levels up to 1 % is not covered by the numerical simulation. This might be due to reduction of parameters that are represented by random fields. Second, even though the composite material does not show explicitly ideal plasticity, the plastic deformation within the numerical simulations starts at higher strain levels as indicated by the experimental results. This might be resolved by reducing the yield strength locally or taking into account hardening effects.

The modeling approach is further endorsed by the results on the right hand side by two important aspects. First, the modeling approach leads to a plastic deformation covering the whole specimen and hence, does not show localized plastic deformation. Second, when dividing the measurement length into small sections, each section show a slightly different behavior. Both phenomena are confirmed by the experimental investigation.

All in all, it can be stated, that the presented modeling approach is a very appropriate method to incorporate the spatial distribution of the elastic and plastic material properties of SFRC.

6. Summary and conclusion

In this work a probabilistic modeling approach for the elasto-plastic material behavior at finite strain based on second-order Gaussian random fields is introduced. The description of the material behavior is based on the Kröner-Lee decomposition. Following this, the strain-energy density function introduced by Bonet et al. [57] is combined with a classical J_2-plasticity formulation assuming ideal plastic behavior. Since this material model is not available in commercially available finite element codes, first an algorithm covering transversely-isotropic elastic-ideal plastic material behavior is developed and implemented in COMSOL Multiphysics®. The validation based on the well-known Neo-Hookean material model in the elastic and plastic domain as well as utilizing a user-defined strain-energy density function in the elastic domain show an excellent conformity.

Therefore, in a second step, based on the correlation analysis done in a previous study [24] cross-correlated second-order Gaussian random fields are generated to represent

 doi:10.20944/preprints202209.0088.v1

spatial distribution the strain-energy density function parameter Λ and the yield strength induced by the probabilistic characteristics of the microstructure. The remaining parameters are assumed to be homogeneous at this state of the study. With the spatially distributed material properties tensile tests for specimens made of PBT-GF-30 are simulated. Even though the initial modeling approach is based on elastic-ideal plastic material behavior the spatial distribution of two material parameters leads to localized plastic deformation covering the whole measurement length. This causes a strain dependent reduction of the material stiffness.

To validate the numerical results and the presented modeling approach uniaxial tensile tests are conducted to characterize the elastic and plastic deformation of PBT-GF-30. The obtained stress-strain curves are compared to the numerical results. It is shown that with an decreasing correlation length the numerical data matches the experimental results quite well. The deviation at large strain can be assigned to assumption of ideal plasticity. Furthermore, this initial investigation does not show a significant deviation between the results of different realizations at a low strain level. The reasons are the reduction of complexity by representing only one parameter of the strain-energy density function by a random field and the limitation of Gaussian random fields. To ensure only positive values for the yield strength low values are underestimated.

Summarizing, it can be concluded that the presented initial probabilistic approach is suitable for the numerical simulation of the elasto-plastic material behavior of SFRC at finite strain including its spatial distribution on the component level without the need of an explicit microstructural modeling. Future work will focus on the implementation of specimen unloading, hardening, non-Gaussian random fields and the representation of additional parameters by stochastic methods.

Funding: The financial support of the German Academic Exchange Service (Grant No. 91789376) is gratefully acknowledged.

Institutional Review Board Statement: Not applicable.

Informed Consent Statement: Not applicable.

Data Availability Statement: The data presented in this study is available on request from the corresponding author.

Acknowledgments: I want to acknowledge and extend my sincere thanks to Celia Reina for the valuable ideas and tips during our discussions that significantly improved and shaped the work.

Conflicts of Interest: The author declare no conflict of interest. The funders had no role in the design of the study; in the collection, analyses, or interpretation of data; in the writing of the manuscript, or in the decision to publish the results.

Abbreviations

The following abbreviations are used in this manuscript:

EOLE	expansion optimal linear estimate
FEM	Finite element method
KLE	Karhunen-Loève expansion
mcKL	Multiple correlated Karhunen-Loève expansion
muKL	Multiple uncorrelated Karhunen-Loève expansion
PBT	Polybutylene terephthalate
RVE	Representative volume element
SFRC	Short fiber-reinforced composite
std	Standard deviation

Appendix A

For the implementation of the elastic-ideal plastic routine in COMSOL Multiphysics® several subroutines are used to calculate the second Piola-Kirchhoff stress tensor in the

Preprints (www.preprints.org) | NOT PEER-REVIEWED | Posted: 6 September 2022 doi:10.20944/preprints202209.0088.v1

Table A1. List of input and output arguments for Algorithm A1 (CALCS_INTERMEDIATE).

Variable	Symbol	Description
`Cel`	$\bar{\mathbf{C}}_{\text{el}}$	Input: Elastic part of right Cauchy-Green tensor
`lam`	Λ	Input: Material parameter
`mu`	μ	Input: Material parameter
`alpha`	α	Input: Material parameter
`beta`	β	Input: Material parameter
`gamma`	γ	Input: Material parameter
`tol_inv`	–	Input: Tolerance for numerical matrix inversion
`S`	$\bar{\mathbf{S}}$	Output: Second Piola-Kirchhoff stress tensor with respect to the intermediate configuration

Table A2. List of input and output arguments for Algorithm A2 (CALCNORMM).

Variable	Symbol	Description
`F`	$\mathbf{F}$	Input: Deformation gradient
`Fpl`	$\mathbf{F}_{\text{pl}}$	Input: Plastic part of deformation gradient
`Mdev`	$\bar{\mathbf{M}}_{\text{dev}}$	Input: Deviatoric part of Mandel stress with respect to the intermediate configuration
`lam`	Λ	Input: Material parameter
`mu`	μ	Input: Material parameter
`alpha`	α	Input: Material parameter
`beta`	β	Input: Material parameter
`gamma`	γ	Input: Material parameter
`tol_inv`	–	Input: Tolerance for numerical matrix inversion
`dnormx`	$\|\|\bar{\mathbf{M}}_{\text{dev}}\|\|$	Output: Norm of deviatoric part of Mandel stress with respect to the intermediate configuration

intermediate and reference configuration, respectively. Furthermore, the subroutine to calculate the exponential functions `matexp` provided by Hashiguchi et al. [55] written in Fortran is transferred into C. Beside this subroutines COMSOL Multiphysics® provides a library of utility functions for various tensor operations, computing principle and equivalent stresses. These routines are not explained here, a detailed overview is given in the documentation [79].

Table A3. List of input and output arguments for Algorithm A3 (CALC_DEV).

Variable	Symbol	Description
`dp`	$\Delta\lambda$	Input: Plastic multipier
`F`	$\mathbf{F}$	Input: Deformation gradient
`Fpl`	$\mathbf{F}_{\text{pl}}$	Input: Plastic part of deformation gradient
`lam`	Λ	Input: Material parameter
`mu`	μ	Input: Material parameter
`alpha`	α	Input: Material parameter
`beta`	β	Input: Material parameter
`gamma`	γ	Input: Material parameter
`sigYs`	σ_{yield}	Input: Yield stress
`dev`	f_{yield}	Output: Value of yield function

Preprints (www.preprints.org) | NOT PEER-REVIEWED | Posted: 6 September 2022 doi:10.20944/preprints202209.0088.v1

Algorithm A1 Subroutine implemented in COMSOL Multiphysics® for the calculation of $\bar{\mathbf{S}}$

procedure CALCS_INTERMEDIATE(see Table A1)
  compute fiber orientation matrix $\mathbf{A} = \mathbf{a}\mathbf{a}^{\mathrm{T}}$
  compute J, $\bar{\mathbf{C}}_{\mathrm{el}}^{-1}$, $\det \bar{\mathbf{C}}_{\mathrm{el}}$, $\mathrm{tr}\, \bar{\mathbf{C}}_{\mathrm{el}}$, and I_4 ▷ Eqs. (21), (22), and (40)
  compute $\bar{\mathbf{S}}$ ▷ Eq. (42)
end procedure

Algorithm A2 Subroutine implemented in COMSOL Multiphysics® for the calculation of $||\mathbf{M}_{\mathrm{dev}}||$

procedure CALCNORMM(see Table A2)
  compute fiber orientation vector $\mathbf{a}$ and matrix $\mathbf{A} = \mathbf{a}\mathbf{a}^{\mathrm{T}}$
  compute $\mathbf{F}_{\mathrm{pl}}^{-1}$, $\mathbf{F}_{\mathrm{el}}$ ▷ Eq. (20)
  compute $\mathbf{C}$ ▷ Eq. (51)
  compute $\bar{\mathbf{S}}$ by calling Algorithm A1 ▷ Eq. (42)
  compute $\bar{\mathbf{M}}$ and $\bar{\mathbf{M}}_{\mathrm{dev}}$ ▷ Eq. (32)
  compute $||\bar{\mathbf{M}}_{\mathrm{dev}}||$
end procedure

Algorithm A3 Subroutine implemented in COMSOL Multiphysics® for the evaluation of f_{yield}

procedure CALC_DEV(see Table A2)
  compute $||\bar{\mathbf{M}}_{\mathrm{dev}}||$ by calling Algorithm A2
  compute directional tensor of plastic evolution
  compute tensor exponential by calling Algorithm A4 ▷ Eq. (38)
  update $\mathbf{F}_{\mathrm{pl}}$ ▷ Eq. (37)
  compute $||\bar{\mathbf{M}}_{\mathrm{dev}}||$ by calling Algorithm A2
  evaluate f_{yield} ▷ Eq. (34)
end procedure

Algorithm A4 Subroutine implemented in COMSOL Multiphysics® for the calculation of the tensor exponential function, adapted from Hashiguchi et al. [55]

procedure MATEXP(see Table A3)
  initialize Identity matrix as first element of the series expansion
  initialize `temp` and $\mathbf{A}$
  initialize factorial
  set temp to initial solution
  do
    compute $\mathbf{T}^n$ and its norm
    compute $n!$
    add $\mathbf{T}^n$ to `temp`
    compute current solution by adding n-th order term to $\mathbf{A}$
    check convergence
  while `res` > `tol` and `n` < `nmax`
end procedure

 doi:10.20944/preprints202209.0088.v1

Table A4. List of input and output arguments for Algorithm A4 (MATEXP).

Variable	Symbol	Description
`nmax`	–	Input: Maximum number of terms of the series representation
`etol`	–	Input: Convergence tolerance
`a`	–	Input: Matrix
`aexp`	–	Output: Tensor exponential function

References

1. Ebrahimi, F.; Dabbagh, A. A comprehensive review on modeling of nanocomposite materials and structures. *Journal of Computational Applied Mechanics* **2019**, *50*, 197–209.
2. Rauter, N. A computational modeling approach based on random fields for short fiber-reinforced composites with experimental verification by nanoindentation and tensile tests. *Computational Mechanics* **2021**, *67*, 699–722. https://doi.org/10.1007/s00466-020-01958-3.
3. Hristopulos, D.T. *Random fields for spatial data modeling: A primer for scientists and engineers*; Advances in geographic information science, Springer: Dordrecht, 2020.
4. Maccone, C. *Deep Space Flight and Communications: Exploiting the Sun as a Gravitational Lens*; Springer Praxis Books, Springer Berlin Heidelberg: Berlin, Heidelberg, 2009.
5. Vanmarcke, E. *Random fields: Analysis and synthesis*, rev. and expanded new ed. ed.; World Scientific Publ: Singapore, 2010.
6. Soize, C. Non-Gaussian positive-definite matrix-valued random fields for elliptic stochastic partial differential operators. *Computer Methods in Applied Mechanics and Engineering* **2006**, *195*, 26–64. https://doi.org/10.1016/j.cma.2004.12.014.
7. Soize, C. Tensor-valued random fields for meso-scale stochastic model of anisotropic elastic microstructure and probabilistic analysis of representative volume element size. *Probabilistic Engineering Mechanics* **2008**, *23*, 307–323. https://doi.org/10.1016/j.probengmech.2007.12.019.
8. Guilleminot, J.; Soize, C.; Kondo, D.; Binetruy, C. Theoretical framework and experimental procedure for modelling mesoscopic volume fraction stochastic fluctuations in fiber reinforced composites. *International Journal of Solids and Structures* **2008**, *45*, 5567–5583. https://doi.org/10.1016/j.ijsolstr.2008.06.002.
9. Guilleminot, J.; Soize, C.; Kondo, D. Mesoscale probabilistic models for the elasticity tensor of fiber reinforced composites: Experimental identification and numerical aspects. *Mechanics of Materials* **2009**, *41*, 1309–1322. https://doi.org/10.1016/j.mechmat.2009.08.004.
10. Le, T.T.; Guilleminot, J.; Soize, C. Stochastic continuum modeling of random interphases from atomistic simulations. Application to a polymer nanocomposite. *Computer Methods in Applied Mechanics and Engineering* **2016**, *303*, 430–449. https://doi.org/10.1016/j.cma.2015.10.006.
11. Guilleminot, J.; Soize, C. Non-Gaussian Random Fields in Multiscale Mechanics of Heterogeneous Materials. In *Encyclopedia of Continuum Mechanics*; Altenbach, H.; Öchsner, A., Eds.; Springer Berlin Heidelberg: Berlin, Heidelberg, 2017; pp. 1–9. https://doi.org/10.1007/978-3-662-53605-6{_}68-1.
12. Chen, G.; Suo, X. Constitutive modeling of nonlinear compressive behavior of fiber reinforced polymer composites. *Polymer Composites* **2020**, *41*, 182–190. https://doi.org/10.1002/pc.25358.
13. de Groof, V.; Oberguggenberger, M.; Haller, H.; Degenhardt, R.; Kling, A. A case study of random field models applied to thin-walled composite cylinders in finite element analysis. *Proceedings 11th International Conference on Structural Safety & Reliability* **2013**.
14. Stefanou, G.; Savvas, D.; Metsis, P. Random Material Property Fields of 3D Concrete Microstructures Based on CT Image Reconstruction. *Materials (Basel, Switzerland)* **2021**, *14*. https://doi.org/10.3390/ma14061423.
15. Zimmermann, E.; Eremin, A.; Lammering, R. Analysis of the continuous mode conversion of Lamb waves in fiber composites by a stochastic material model and laser vibrometer experiments. *GAMM-Mitteilungen* **2018**, *41*, e201800001. https://doi.org/10.1002/gamm.201800001.
16. Zheng, K.; Yang, K.; Shi, J.; Yuan, J.; Zhou, G. Innovative methods for random field establishment and statistical parameter inversion exemplified with 6082-T6 aluminum alloy. *Scientific Reports* **2019**, *9*, 17788. https://doi.org/10.1038/s41598-019-54046-9.
17. Huang, H.B.; Huang, Z.M. Micromechanical prediction of elastic-plastic behavior of a short fiber or particle reinforced composite. *Composites Part A: Applied Science and Manufacturing* **2020**, *134*, 105889. https://doi.org/10.1016/j.compositesa.2020.105889.
18. Rauter, N.; Lammering, R. Experimental Characterization of Short Fiber-Reinforced Composites on the Mesoscale by Indentation Tests. *Applied Composite Materials* **2021**. https://doi.org/10.1007/s10443-021-09937-4.
19. Savvas, D.; Stefanou, G.; Papadrakakis, M. Determination of RVE size for random composites with local volume fraction variation. *Computer Methods in Applied Mechanics and Engineering* **2016**, *305*, 340–358. https://doi.org/10.1016/j.cma.2016.03.002.
20. Breuer, K.; Stommel, M. RVE modelling of short fiber reinforced thermoplastics with discrete fiber orientation and fiber length distribution. *SN Applied Sciences* **2020**, *2*, 140. https://doi.org/10.1007/s42452-019-1890-5.
21. Breuer, K.; Stommel, M. Prediction of Short Fiber Composite Properties by an Artificial Neural Network Trained on an RVE Database. *Fibers* **2021**, *9*, 8. https://doi.org/10.3390/fib9020008.
22. Zhang, S.; van Dommelen, J.A.W.; Govaert, L.E. Micromechanical Modeling of Anisotropy and Strain Rate Dependence of Short-Fiber-Reinforced Thermoplastics. *Fibers* **2021**, *9*, 44. https://doi.org/10.3390/fib9070044.
23. Jia, D.; Shi, H.; Cheng, L. Multiscale thermomechanical modeling of short fiber-reinforced composites. *Science and Engineering of Composite Materials* **2017**, *24*, 765–772. https://doi.org/10.1515/secm-2015-0487.
24. Rauter, N. Correlation analysis of the elastic-ideal plastic material behavior of short fiber-reinforced composites. *International Journal for Numerical Methods in Engineering* **2022**, pp. 1–19. https://doi.org/10.1002/nme.7113.
25. Baxter, S.C.; Graham, L.L. Characterization of Random Composites Using Moving-Window Technique. *Journal of Engineering Mechanics* **2000**, *126*, 389–397. https://doi.org/10.1061/(ASCE)0733-9399(2000)126:4(389).

26. Graham-Brady, L.L.; Siragy, E.F.; Baxter, S.C. Analysis of Heterogeneous Composites Based on Moving-Window Techniques. *Journal of Engineering Mechanics* **2003**, *129*, 1054–1064. https://doi.org/10.1061/(ASCE)0733-9399(2003)129:9(1054).
27. Ponte Castañeda, P. The effective mechanical properties of nonlinear isotropic composites. *Journal of the Mechanics and Physics of Solids* **1991**, *39*, 45–71. https://doi.org/10.1016/0022-5096(91)90030-R.
28. Ponte Castañeda, P. Stationary variational estimates for the effective response and field fluctuations in nonlinear composites. *Journal of the Mechanics and Physics of Solids* **2016**, *96*, 660–682. https://doi.org/10.1016/j.jmps.2016.06.010.
29. Chemie Wirtschaftsförderungsgesellschaft mbH. CAMPUS® Datasheet: Ultradur® B 4300 G6 - PBT-GF30. https://www.campusplastics.com/material/pdf/140403/UltradurB4300G6?sLg=en, 2021.
30. International Organization for Standardization. *Plastics – Determination of tensile properties: Part 1: General principles*, ISO 527-1:2019 ed.; International Organization for Standardization: Vernier, Geneva, Switzerland, 2019.
31. Ghanem, R.G. *Stochastic finite elements: A spectral approach*; Springer: New York, 2012.
32. Sudret, B.; Der Kiurghian, A. Stochastic Finite Element Methods and Reliability: A State-of-the-Art Report. Report no. ucb/semm-2000/08, University of California, Berkeley, November 2000.
33. Chu, S.; Guilleminot, J. Stochastic multiscale modeling with random fields of material properties defined on nonconvex domains. *Mechanics Research Communications* **2019**, *97*, 39–45. https://doi.org/10.1016/j.mechrescom.2019.01.008.
34. Guilleminot, J. 12 - Modeling non-Gaussian random fields of material properties in multiscale mechanics of materials. In *Uncertainty Quantification in Multiscale Materials Modeling*; Wang, Y.; McDowell, D.L., Eds.; Elsevier Series in Mechanics of Advanced Materials, Woodhead Publishing, 2020; pp. 385–420. https://doi.org/https://doi.org/10.1016/B978-0-08-102941-1.00012-2.
35. Malyarenko, A.; Ostoja-Starzewski, M. A Random Field Formulation of Hooke's Law in All Elasticity Classes. *Journal of Elasticity* **2017**, *127*, 269–302. https://doi.org/10.1007/s10659-016-9613-2.
36. Tran, V.P. Stochastic modeling of random heterogeneous materials. Dissertation, Université Paris-Est, Paris, 2016.
37. Der Kiureghian, A.; Ke, J.B. The stochastic finite element method in structural reliability. *Probabilistic Engineering Mechanics* **1988**, *3*, 83–91. https://doi.org/10.1016/0266-8920(88)90019-7.
38. Yamazaki, F.; Member, A.; Shinozuka, M.; Dasgupta, G. Neumann Expansion for Stochastic Finite Element Analysis. *Journal of Engineering Mechanics* **1988**, *114*, 1335–1354. https://doi.org/10.1061/(ASCE)0733-9399(1988)114:8(1335).
39. Vanmarcke, E.; Grigoriu, M. Stochastic Finite Element Analysis of Simple Beams. *Journal of Engineering Mechanics* **1983**, *109*, 1203–1214. https://doi.org/10.1061/(ASCE)0733-9399(1983)109:5(1203).
40. Liu, W.K.; Belytschko, T.; Mani, A. Random field finite elements. *International Journal for Numerical Methods in Engineering* **1986**, *23*, 1831–1845. https://doi.org/10.1002/nme.1620231004.
41. Liu, P.L.; Kiureghian, A.D. Finite Element Reliability of Geometrically Nonlinear Uncertain Structures. *Journal of Engineering Mechanics* **1991**, *117*, 1806–1825. https://doi.org/10.1061/(ASCE)0733-9399(1991)117:8(1806).
42. Kamiński, M.; Kleiber, M. Stochastic structural interface defects in fiber composites. *International Journal of Solids and Structures* **1996**, *33*, 3035–3056. https://doi.org/10.1016/0020-7683(95)00264-2.
43. Lawrence, M.A. Basis random variables in finite element analysis. *International Journal for Numerical Methods in Engineering* **1987**, *24*, 1849–1863. https://doi.org/10.1002/NME.1620241004.
44. Spanos, P.D.; Ghanem, R. Stochastic Finite Element Expansion for Random Media. *Journal of Engineering Mechanics* **1989**, *115*, 1035–1053. https://doi.org/10.1061/(ASCE)0733-9399(1989)115:5(1035).
45. Loève, M. *Probability theory*, 4. ed. ed.; Vol. 45, Springer: New York, 1977.
46. Cho, H.; Venturi, D.; Karniadakis, G.E. Karhunen–Loève expansion for multi-correlated stochastic processes. *Probabilistic Engineering Mechanics* **2013**, *34*, 157–167. https://doi.org/10.1016/j.probengmech.2013.09.004.
47. Betz, W.; Papaioannou, I.; Straub, D. Numerical methods for the discretization of random fields by means of the Karhunen–Loève expansion. *Computer Methods in Applied Mechanics and Engineering* **2014**, *271*, 109–129. https://doi.org/10.1016/j.cma.2013.12.010.
48. Ostoja-Starzewski, M. *Microstructural Randomness and Scaling in Mechanics of Materials*; Chapman and Hall/CRC, 2007. https://doi.org/10.1201/9781420010275.
49. Li, C.C.; Der Kiureghian, A. Optimal Discretization of Random Fields. *Journal of Engineering Mechanics* **1993**, *119*, 1136–1154. https://doi.org/10.1061/(ASCE)0733-9399(1993)119:6(1136).
50. Atkinson, K.E. *The Numerical Solution of Integral Equations of the Second Kind*; Cambridge University Press, 2010. https://doi.org/10.1017/CBO9780511626340.
51. Rauter, N.; Lammering, R. Correlation structure in the elasticity tensor for short fiber-reinforced composites. *Probabilistic Engineering Mechanics* **2020**, *62*, 103100. https://doi.org/10.1016/j.probengmech.2020.103100.
52. Golub, G.H.; van Loan, C.F. *Matrix computations*; Johns Hopkins studies in the mathematical sciences, Johns Hopkins Univ. Press: Baltimore, 2007.
53. Ghanem, R.G.; Spanos, P.D. Polynomial Chaos in Stochastic Finite Elements. *Journal of Applied Mechanics* **1990**, *57*, 197–202. https://doi.org/10.1115/1.2888303.
54. Simo, J.C.; Hughes, T.J.R. *Computational inelasticity*; Vol. v. 7, *Interdisciplinary applied mathematics*, Springer: New York, 1998.
55. Hashiguchi, K. *Introduction to finite strain theory for continuum elasto-plasticity*, online-ausg ed.; Wiley series in computational mechanics, Wiley: Chichester, West Sussek, U.K, 2012.

56. Eidel, B.; Gruttmann, F. Elastoplastic orthotropy at finite strains: multiplicative formulation and numerical implementation. *Computational Materials Science* **2003**, *28*, 732–742. https://doi.org/10.1016/j.commatsci.2003.08.027.
57. Bonet, J.; Burton, A.J. A simple orthotropic, transversely isotropic hyperelastic constitutive equation for large strain computations. *Computer Methods in Applied Mechanics and Engineering* **1998**, *162*, 151–164. https://doi.org/10.1016/S0045-7825(97)00339-3.
58. Kröner, E. Allgemeine Kontinuumstheorie der Versetzungen und Eigenspannungen. *Archive for Rational Mechanics and Analysis* **1959**, *4*, 273–334. https://doi.org/10.1007/BF00281393.
59. Lee, E.H.; Liu, D.T. Finite–Strain Elastic–Plastic Theory with Application to Plane–Wave Analysis. *Journal of Applied Physics* **1967**, *38*, 19–27. https://doi.org/10.1063/1.1708953.
60. Lee, E.H. Elastic-Plastic Deformation at Finite Strains. *Journal of Applied Mechanics* **1969**, *36*, 1–6. https://doi.org/10.1115/1.3564580.
61. Mandel, J. Director vectors and constitutive equations for plastic and visco-plastic media. In *Problems of Plasticity*; Sawczuk, A., Ed.; Springer Netherlands: Dordrecht, 1974; Vol. 4, pp. 135–143. https://doi.org/10.1007/978-94-010-2311-5{_}6.
62. Lubarda, V.A. *Elastoplasticity Theory*; CRC PRESS: Boca Raton, 2019.
63. Vladimirov, I.N.; Pietryga, M.P.; Reese, S. On the modelling of non–linear kinematic hardening at finite strains with application to springback—Comparison of time integration algorithms. *International Journal for Numerical Methods in Engineering* **2008**, *75*, 1–28. https://doi.org/10.1002/nme.2234.
64. Miehe, C. Exponential map algorithm for stress updates in anisotropic multiplicative elastoplasticity for single crystals. *International Journal for Numerical Methods in Engineering* **1996**, *39*, 3367–3390. https://doi.org/10.1002/(SICI)1097-0207(19961015)39:19{\T1\textless}3367::AID-NME4{\T1\textgreater}3.0.CO;2-7.
65. Simo, J.C.; Ortiz, M. A unified approach to finite deformation elastoplastic analysis based on the use of hyperelastic constitutive equations. *Computer Methods in Applied Mechanics and Engineering* **1985**, *49*, 221–245. https://doi.org/10.1016/0045-7825(85)90061-1.
66. Simo, J.C. A framework for finite strain elastoplasticity based on maximum plastic dissipation and the multiplicative decomposition. Part II: Computational aspects. *Computer Methods in Applied Mechanics and Engineering* **1988**, *68*, 1–31. https://doi.org/10.1016/0045-7825(88)90104-1.
67. Simo, J.C. A framework for finite strain elastoplasticity based on maximum plastic dissipation and the multiplicative decomposition: Part I. Continuum formulation. *Computer Methods in Applied Mechanics and Engineering* **1988**, *66*, 199–219. https://doi.org/10.1016/0045-7825(88)90076-X.
68. Altenbach, H. *Kontinuumsmechanik*; Springer Berlin Heidelberg: Berlin, Heidelberg, 2015. https://doi.org/10.1007/978-3-662-47070-1.
69. Malvern, L.E. *Introduction to the mechanics of a continuous medium*; Prentice-Hall series in engineering of the physical sciences, Prentice-Hall: Englewood Cliffs, NJ, 1969.
70. Holzapfel, G.A. *Nonlinear solid mechanics: A continuum approach for engineering*, reprinted with corrections ed.; John Wiley & Sons LTD: Chichester and Weinheim and New York and Brisbane and Singapore and Toronto, 2000.
71. Spencer, A.J.M. *Deformations of fibre-reinforced materials*; Oxford science research papers, Clarendon Press: Oxford, 1972.
72. Miehe, C. Numerical computation of algorithmic (consistent) tangent moduli in large-strain computational inelasticity. *Computer Methods in Applied Mechanics and Engineering* **1996**, *134*, 223–240. https://doi.org/10.1016/0045-7825(96)01019-5.
73. Menzel, A.; Steinmann, P. On the spatial formulation of anisotropic multiplicative elasto-plasticity. *Computer Methods in Applied Mechanics and Engineering* **2003**, *192*, 3431–3470. https://doi.org/10.1016/S0045-7825(03)00353-0.
74. Menzel, A.; Ekh, M.; Runesson, K.; Steinmann, P. A framework for multiplicative elastoplasticity with kinematic hardening coupled to anisotropic damage. *International Journal of Plasticity* **2005**, *21*, 397–434. https://doi.org/10.1016/j.ijplas.2003.12.006.
75. Belytschko, T.; Liu, W.K.; Moran, B. *Nonlinear finite elements for continua and structures*, repr ed.; Wiley: Chichester, 2003.
76. Rauter, N.; Lammering, R. The impact of fiber properties on the material coefficients of short fiber-reinforced composites. *PAMM* **2020**, *20*, e202000019. https://doi.org/10.1002/pamm.202000019.
77. Gandhi, U.N.; Goris, S.; Osswald, T.A.; Song, Y.Y. *Discontinuous fiber-reinforced composites: Fundamentals and applications*; Hanser Publishers and Hanser Publications: Munich and Cincinnati, OH, 2020.
78. Rolland, H.; Saintier, N.; Robert, G. Fatigue Mechanisms Description in Short Glass Fiber Reinforced Thermoplastic by Microtomographic Observation. *Proceedings 20th International Conference on Composite Material* **2015**.
79. *Structural Mechanics Module User's Guide*; COMSOL Multiphysics® v. 5.5. COMSOL AB: Stockholm, Schweden, 2019.